An Excitation-Aware and Self-Adaptive Frequency Normalization for Low-Frequency Stabilized Electric Field Integral Equation Formulations

An Excitation-Aware and Self-Adaptive Frequency Normalization for Low-Frequency Stabilized Electric Field Integral Equation Formulations

Bernd Hofmann, *Graduate Student Member, IEEE,* Thomas F. Eibert, *Senior Member, IEEE,* Francesco P. Andriulli, *Senior Member, IEEE,* and Simon B. Adrian, *Member, IEEE*

***Abstract*—The accurate solution of quasi-Helmholtz decomposed electric field integral equations (EFIEs) in the presence of arbitrary excitations is addressed: Depending on the specific excitation, the quasi-Helmholtz components of the induced current density do not have the same asymptotic scaling in frequency, and thus, the current components are solved for with, in general, different relative accuracies. In order to ensure the same asymptotic scaling, we propose a frequency normalization scheme of quasi-Helmholtz decomposed EFIEs which adapts itself to the excitation and which is valid irrespective of the specific excitation and irrespective of the underlying topology of the structure. Specifically, neither an ad-hoc adaption nor *a-priori* information about the excitation is needed as the scaling factors are derived based on the norms of the right-hand side (RHS) components and the frequency. Numerical results corroborate the presented theory and show the effectiveness of our approach.**

***Index Terms*—Broadband, EFIE, integral equations, loop-star, loop-tree, low frequency, multiply connected, near field, quasi-Helmholtz projectors.**

I. Introduction

THE electric field integral equation (EFIE) constitutes a flexible and accurate formulation for electromagnetic radiation and scattering problems. Preconditioning the discretized equation based on quasi-Helmholtz decompositions is among the most mature approaches to cure an otherwise occurring low-frequency breakdown [1]–[4] (i.e., the condition number increases with decreasing frequency) and enables accurate solutions also for low frequencies down to the static limit. For example, this has been demonstrated for the approach based on quasi-Helmholtz projectors proposed in [5], an enhancement to the explicit decompositions based on a loop-star or loop-tree basis [1]–[4], [6]–[8].

Yet, ensuring that the system matrix is well-conditioned is insufficient if one desires to accurately compute the fields. Two more aspects must be carefully addressed: First, testing the right-hand side (RHS) with solenoidal functions, which is needed for the considered decompositions, can lead to catastrophic round-off errors. Different means to overcome this issue have been proposed [9]–[12] and in the following, it is assumed that a corresponding stabilization is applied since all further derivations rely on an accurately discretized RHS reflecting the physically correct asymptotic scalings in frequency of the quasi-Helmholtz components.

The second problem is addressed in this contribution: It has to be ensured that all quasi-Helmholtz components of the decomposed surface current density, that is, the solenoidal and the non-solenoidal component, are recovered accurately enough to obtain accurate scattered and radiated fields [5], [13]. More precisely, the unknown vector of the linear system of equations (LSE) to be solved has two contributions (i.e, the solenoidal and the non-solenoidal quasi-Helmholtz component), which can differ largely in their order of magnitude. This is due to the, in general, different asymptotic scaling of the quasi-Helmholtz components in the wavenumber k as $k \to 0$, where the specific behavior is dependent on the excitation source. Still both contributions need to be determined accurately.[1]

As the employed preconditioners entail a rescaling of the quasi-Helmholtz decomposed expansion and basis functions, they enforce a different scaling of the quasi-Helmholtz components of the preconditioned current (i.e., the unknown vector) compared to the physical (non-rescaled) one. The same is true for the RHS components. Different choices for the corresponding scaling coefficients have been employed in the past. Typical choices are, for example, given in [2], [5], [19]–[21]. While they are suitable for plane-wave excitations, for arbitrary excitations it is in general not ensured that all components can be recovered as the choices in these existing schemes do not reflect the scaling of the quasi-Helmholtz components of the excitation [22]. Yet, excitations such as voltage gaps are commonly used, and thus, the EFIE should be solved accurately for these as well. The same is true for spherical waves, which are able to represent the field radiated by antennas, or line currents representing radiation from wire structures.

A remedy is using ad-hoc techniques as done in [5]. However, it constitutes an approximation which limits the

Manuscript received Month xx, 2022; revised Month xx, 20XX. Simon B. Adrian was supported by the Deutsche Forschungsgemeinschaft (DFG, German Research Foundation) - SFB 1270/2 – 299150580.

B. Hofmann, and T. F. Eibert are with the Department of Electrical Engineering, School of Computation, Information and Technology, Technical University of Munich, 80290 Munich, Germany (e-mail: bernd.hofmann@tum.de).

F. P. Andriulli is with the Department of Electronics and Telecommunications, Politecnico di Torino, 10129 Turin, Italy.

S. B. Adrian is with the Fakultät für Informatik und Elektrotechnik, Universität Rostock, 18059 Rostock, Germany.

Digital Object Identifier

[1]An investigation whether similar problems occur also for other proposed low-frequency stabilization schemes for scattering and radiation problems such as the augmented EFIE or potential-based approaches [14]–[18] is beyond the scope of this work.

overall accuracy and the behaviour of the quasi-Helmholtz components of the excitation needs to be known a-priori. Moreover, in [5] only three types of excitations were studied (plane wave, capacitive gap excitation, and inductive gap excitation). For other excitations such as spherical TM or TE waves, we find, however, that the approach is not applicable.

In this work, we propose a frequency normalization scheme which adapts itself to the excitation requiring neither a-priori information nor ad-hoc adaptions. To this end, the scaling coefficients incorporate the norms of the quasi-Helmholtz components of the discretized right-hand side in a black-box like manner. Hence, the approach is agnostic to the specific excitation (and the topology of the structure). More precisely, the scaling coefficients are determined such that all quasi-Helmholtz components of the preconditioned current and of the RHS have the same asymptotic scaling. Thereby, all components are recovered with a similar relative accuracy ensuring that all radiated and scattered fields can be computed accurately. Numerical results corroborate the effectiveness of our approach both for canonical and complex geometries. Note that some preliminary results were presented in [22], [23].

This article is organized as follows: Section II introduces background material and fixes the notation. In Section III, the implications of the frequency normalization in quasi-Helmholtz decompositions of the EFIE are analyzed; from the gained insights, the adaptive normalization scheme is derived for the loop-star decomposition as well as for the quasi-Helmholtz projectors. In Section IV, we show how to achieve positive eigenvalues of the preconditioned system matrix, again for both decompositions, and implementation specific aspects are addressed. Numerical studies are presented in Section V.

II. Quasi-Helmholtz Decomposed Electric Field Integral Equations

Let a perfectly electrically conducting (PEC) object with surface Γ be embedded in a homogeneous background medium with permittivity ε and permeability μ. The structure is excited by a time-harmonic field $(\boldsymbol{e}^{\mathrm{ex}}, \boldsymbol{h}^{\mathrm{ex}})$ resulting in an induced surface current density $\boldsymbol{j}$ on Γ from which the scattered or radiated fields can be computed. The current density satisfies the EFIE [24]

$$(\boldsymbol{\mathcal{T}}\boldsymbol{j})_{\tan} = \boldsymbol{e}^{\mathrm{ex}}_{\tan}\,, \tag{1}$$

where[2] $\boldsymbol{\mathcal{T}}\boldsymbol{j} = \mathrm{j}k\boldsymbol{\mathcal{T}}_{\mathrm{A}}\boldsymbol{j} + \mathrm{j}k^{-1}\boldsymbol{\mathcal{T}}_{\Phi}\boldsymbol{j}$ contains the vector potential operator

$$\boldsymbol{\mathcal{T}}_{\mathrm{A}}\boldsymbol{j} = \iint_{\Gamma} G(\boldsymbol{r},\boldsymbol{r}')\,\boldsymbol{j}(\boldsymbol{r}')\,\mathrm{d}S(\boldsymbol{r}') \tag{2}$$

and the scalar potential operator

$$\boldsymbol{\mathcal{T}}_{\Phi}\boldsymbol{j} = \nabla \iint_{\Gamma} G(\boldsymbol{r},\boldsymbol{r}')\,\nabla_{\Gamma}\cdot\boldsymbol{j}(\boldsymbol{r}')\,\mathrm{d}S(\boldsymbol{r}') \tag{3}$$

[2]Note, that the choice of defining $\boldsymbol{\mathcal{T}}$ without a surface normal vector $\hat{\boldsymbol{n}}$ is independent of the considered low-frequency stabilization and the proposed scheme. However, it has the advantage that non-orientable surfaces (which do not possess a canonically definable normal vector field) can be considered as scattering objects in a natural manner [25], [26].

with the free-space Green's function

$$G(\boldsymbol{r},\boldsymbol{r}') = \frac{\mathrm{e}^{-\mathrm{j}k|\boldsymbol{r}-\boldsymbol{r}'|}}{4\pi|\boldsymbol{r}-\boldsymbol{r}'|}, \tag{4}$$

the wavenumber $k = \omega\sqrt{\mu\varepsilon}$, the angular frequency ω, and the imaginary unit $\mathrm{j}^2 = -1$. Moreover, an implicit normalization of the current with respect to the wave impedance is assumed as well as a suppressed time dependency of $\mathrm{e}^{\mathrm{j}\omega t}$. To solve for $\boldsymbol{j}$, the surface Γ is triangulated and $\boldsymbol{j}$ is expanded with Rao-Wilton-Glisson (RWG) functions $\boldsymbol{f}_n$ as $\boldsymbol{j} \approx \sum_{n=1}^{N} [\boldsymbol{j}]_n \boldsymbol{f}_n(\boldsymbol{r})$, where $\boldsymbol{j} \in \mathbb{C}^N$ contains the unknown expansion coefficients. Employing the $\boldsymbol{f}_n$ as testing functions in a ~~Petrov-~~Galerkin scheme, results in the LSE

$$\boldsymbol{T}\boldsymbol{j} = (\mathrm{j}k\boldsymbol{T}_{\mathrm{A}} + \mathrm{j}k^{-1}\boldsymbol{T}_{\Phi})\boldsymbol{j} = \boldsymbol{e}^{\mathrm{ex}}\,, \tag{5}$$

where the matrix $\boldsymbol{T}_{\mathrm{A}} \in \mathbb{C}^{N\times N}$ exhibits the entries $[\boldsymbol{T}_{\mathrm{A}}]_{mn} = \iint_{\Gamma} \boldsymbol{f}_m \cdot \boldsymbol{\mathcal{T}}_{\mathrm{A}}\boldsymbol{f}_n\,\mathrm{d}S(\boldsymbol{r})$, the matrix $\boldsymbol{T}_{\Phi} \in \mathbb{C}^{N\times N}$ exhibits the entries $[\boldsymbol{T}_{\Phi}]_{mn} = \iint_{\Gamma} \boldsymbol{f}_m \cdot \boldsymbol{\mathcal{T}}_{\Phi}\boldsymbol{f}_n\,\mathrm{d}S(\boldsymbol{r})$ (to be evaluated in a weak sense), and the RHS vector $\boldsymbol{e}^{\mathrm{ex}} \in \mathbb{C}^N$ exhibits the entries $[\boldsymbol{e}^{\mathrm{ex}}]_m = \iint_{\Gamma} \boldsymbol{f}_m \cdot \boldsymbol{e}^{\mathrm{ex}}\,\mathrm{d}S(\boldsymbol{r})$.

To address the low-frequency breakdown of the EFIE, we consider as first approach the loop-star decomposition. It allows to carry out the analysis in a demonstrative way before adapting it to the second and actual decomposition of interest: quasi-Helmholtz projectors.

A. Loop-Star Decomposition

The well known [3], [4], [6] basic idea of the loop-star decomposition is to express the current density $\boldsymbol{j}$ as a superposition of N_Λ local loops $\boldsymbol{\Lambda}_m$ and N_H global loops $\boldsymbol{H}_m$ (associated with the handles and holes of Γ) representing the solenoidal component of $\boldsymbol{j}$, as well as N_Σ stars $\boldsymbol{\Sigma}_m$ representing the non-solenoidal component of $\boldsymbol{j}$. To do so, the loop to RWG expansion coefficient mapping matrix $\boldsymbol{\Lambda} \in \mathbb{R}^{N\times N_\Lambda}$, the global loop to RWG expansion coefficient mapping matrix $\boldsymbol{H} \in \mathbb{R}^{N\times N_H}$, and the star to RWG expansion coefficient mapping matrix $\boldsymbol{\Sigma} \in \mathbb{R}^{N\times N_\Sigma}$ all as defined in [8] are introduced. Applying the transformation matrix $\boldsymbol{Q} = [\boldsymbol{\Lambda}\ \boldsymbol{H}\ \boldsymbol{\Sigma}]$ to (5) as $\boldsymbol{T}_{\Lambda H\Sigma}\boldsymbol{j}'' = \boldsymbol{Q}^{\mathrm{T}}\boldsymbol{T}\boldsymbol{Q}\boldsymbol{j}'' = \boldsymbol{Q}^{\mathrm{T}}\boldsymbol{e}^{\mathrm{ex}}$, where $\boldsymbol{j} = \boldsymbol{Q}\boldsymbol{j}''$, allows to remove the ill-conditioning of (5) with respect to k by introducing suitable diagonal block normalization matrices $\boldsymbol{D}_1$ and $\boldsymbol{D}_2$ yielding the stabilized system

$$\boldsymbol{D}_1\boldsymbol{T}_{\Lambda H\Sigma}\boldsymbol{D}_2\boldsymbol{j}' = \boldsymbol{D}_1\boldsymbol{Q}^{\mathrm{T}}\boldsymbol{e}^{\mathrm{ex}} \tag{6}$$

with $\boldsymbol{j} = \boldsymbol{Q}\boldsymbol{D}_2\boldsymbol{j}'$. Common choices in literature for these matrices are $\boldsymbol{D}_1 = \boldsymbol{D}_2 = (1,1,k)$ [2], $\boldsymbol{D}_1 = \boldsymbol{D}_2 = \mathrm{diag}(1/\sqrt{k}, 1/\sqrt{k}, \sqrt{k})$ [5], or $\boldsymbol{D}_1 = \mathrm{diag}(1/k, 1/k, 1)$ and $\boldsymbol{D}_2 = \mathrm{diag}(1,1,k)$ [19]. Here, we define it in a general form as

$$\boldsymbol{D}_i = \mathrm{diag}(\alpha_i, \gamma_i, \beta_i) \tag{7}$$

and systematically derive the coefficients α_i, γ_i, and β_i to suit arbitrary excitations. Consequently, the preconditioned system (6) is solved for $\boldsymbol{j}' = [\boldsymbol{j}_\Lambda^{\mathrm{T}}\ \boldsymbol{j}_H^{\mathrm{T}}\ \boldsymbol{j}_\Sigma^{\mathrm{T}}]^{\mathrm{T}}$ which is related to the actual current vector as

$$\boldsymbol{j} = \alpha_2\boldsymbol{\Lambda}\boldsymbol{j}_\Lambda + \gamma_2\boldsymbol{H}\boldsymbol{j}_H + \beta_2\boldsymbol{\Sigma}\boldsymbol{j}_\Sigma\,. \tag{8}$$

Table I
NOTATION OVERVIEW.

	loop-star	projectors
$\boldsymbol{j}'_{\mathrm{sol}} :=$	$\boldsymbol{\Lambda} j_{\Lambda}$	$\boldsymbol{P}_{\Lambda}\boldsymbol{j}'$
$\boldsymbol{j}'_{\mathrm{hsol}} :=$	$\boldsymbol{H} j_{H}$	$\boldsymbol{P}_{H}\boldsymbol{j}'$
$\boldsymbol{j}'_{\mathrm{nsol}} :=$	$\boldsymbol{\Sigma} j_{\Sigma}$	$\boldsymbol{P}_{\Sigma}\boldsymbol{j}'$
$\boldsymbol{j}_{\mathrm{sol}} :=$	$\alpha_2 \boldsymbol{j}'_{\mathrm{sol}}$	
$\boldsymbol{j}_{\mathrm{hsol}} :=$	$\gamma_2 \boldsymbol{j}'_{\mathrm{hsol}}$	
$\boldsymbol{j}_{\mathrm{nsol}} :=$	$\beta_2 \boldsymbol{j}'_{\mathrm{nsol}}$	

	loop-star	projectors
$\boldsymbol{e}_{\mathrm{sol}} :=$	$\boldsymbol{\Lambda}^{\mathrm{T}}\boldsymbol{e}^{\mathrm{ex}}$	$\boldsymbol{P}_{\Lambda}\boldsymbol{e}^{\mathrm{ex}}$
$\boldsymbol{e}_{\mathrm{hsol}} :=$	$\boldsymbol{H}^{\mathrm{T}}\boldsymbol{e}^{\mathrm{ex}}$	$\boldsymbol{P}_{H}\boldsymbol{e}^{\mathrm{ex}}$
$\boldsymbol{e}_{\mathrm{nsol}} :=$	$\boldsymbol{\Sigma}^{\mathrm{T}}\boldsymbol{e}^{\mathrm{ex}}$	$\boldsymbol{P}_{\Sigma}\boldsymbol{e}^{\mathrm{ex}}$
$\boldsymbol{e}'_{\mathrm{sol}} :=$	$\alpha_1 \boldsymbol{e}_{\mathrm{sol}}$	
$\boldsymbol{e}'_{\mathrm{hsol}} :=$	$\gamma_1 \boldsymbol{e}_{\mathrm{hsol}}$	
$\boldsymbol{e}'_{\mathrm{nsol}} :=$	$\beta_1 \boldsymbol{e}_{\mathrm{nsol}}$	

B. Quasi-Helmholtz Projectors

As an improvement over the loop-star decomposition, the quasi-Helmholtz projectors introduced in [5] can be employed: The orthogonal projectors $\boldsymbol{P}_{\Sigma} \in \mathbb{R}^{N\times N}$ defined by $\boldsymbol{P}_{\Sigma} = \boldsymbol{\Sigma}(\boldsymbol{\Sigma}^{\mathrm{T}}\boldsymbol{\Sigma})^{+}\boldsymbol{\Sigma}^{\mathrm{T}}$, where $(\cdot)^{+}$ denotes the Moore-Penrose pseudoinverse, $\boldsymbol{P}_{\Lambda} \in \mathbb{R}^{N\times N}$ defined by $\boldsymbol{P}_{\Lambda} = \boldsymbol{\Lambda}(\boldsymbol{\Lambda}^{\mathrm{T}}\boldsymbol{\Lambda})^{+}\boldsymbol{\Lambda}^{\mathrm{T}}$, and $\boldsymbol{P}_{H} \in \mathbb{R}^{N\times N}$ defined by $\boldsymbol{P}_{H} = \mathsf{I} - \boldsymbol{P}_{\Lambda} - \boldsymbol{P}_{\Sigma}$ are introduced (note that the pseudoinverses can be computed efficiently via algebraic multigrid (AMG) preconditioning as detailed in [5, Section V]) as well as the decomposition operator

$$\boldsymbol{P}_i = \alpha_i \boldsymbol{P}_{\Lambda} + \gamma_i \boldsymbol{P}_{H} + \beta_i \boldsymbol{P}_{\Sigma} \,. \tag{9}$$

Applying the latter to (5) as

$$\boldsymbol{P}_1 \boldsymbol{T} \boldsymbol{P}_2 \boldsymbol{j}' = \boldsymbol{P}_1 \boldsymbol{e}^{\mathrm{ex}} \tag{10}$$

yields a well-conditioned LSE, which is better conditioned than (6), with

$$\boldsymbol{j} = \boldsymbol{P}_2 \boldsymbol{j}' = \alpha_2 \boldsymbol{P}_{\Lambda}\boldsymbol{j}' + \gamma_2 \boldsymbol{P}_{H}\boldsymbol{j}' + \beta_2 \boldsymbol{P}_{\Sigma}\boldsymbol{j}' \tag{11}$$

if α_i, β_i, and γ_i, $i = 1, 2$ are suitably chosen; specifically, in [5], a combined projector, $\boldsymbol{P}_{\Lambda H} = \boldsymbol{P}_{\Lambda} + \boldsymbol{P}_{H}$ is used with $\alpha_1 = \alpha_2 = \gamma_1 = \gamma_2 = 1/\sqrt{k}$ and $\beta_1 = \beta_2 = \mathrm{j}\sqrt{k}$. In contrast, we chose with our definition of $\boldsymbol{P}_i$ to treat $\boldsymbol{P}_{\Lambda}$ and $\boldsymbol{P}_{H}$ separately as we need the general form for our theoretical apparatus. Our final formulation uses again the combined projector $\boldsymbol{P}_{\Lambda H}$.

For both decompositions, we define the quasi-Helmholtz components $\boldsymbol{j}'_{\mathrm{sol}}$, $\boldsymbol{j}'_{\mathrm{hsol}}$, and $\boldsymbol{j}'_{\mathrm{nsol}}$, that is, the solenoidal component, the solenoidal component associated with the handles and holes of Γ, and the non-solenoidal component, respectively, as shown in Table I. This leads to the preconditioner-agnostic definitions of $\boldsymbol{j}_{\mathrm{sol}}$, $\boldsymbol{j}_{\mathrm{hsol}}$, and $\boldsymbol{j}_{\mathrm{nsol}}$. Moreover, we introduce $\boldsymbol{j}_{\mathrm{sol,hsol}} = \boldsymbol{j}_{\mathrm{sol}} + \boldsymbol{j}_{\mathrm{hsol}}$. The RHS Helmholtz components $\boldsymbol{e}_{\mathrm{sol}}$, $\boldsymbol{e}_{\mathrm{hsol}}$, $\boldsymbol{e}_{\mathrm{nsol}}$, as well as their primed variants are defined analogously.

Moreover, note that in order to also cure the dense-discretization breakdown of the EFIE (i.e., the ill-conditioning with respect to the average edge length of the triangulation of Γ), formulation (10) could be combined with a Calderón preconditioner similar to what has been done using the standard choice of scaling coefficients in [5], [27]. While such a combination should be compatible with the here proposed frequency normalization scheme, further investigations would be necessary which are beyond the scope of this work.

III. Analysis of the Frequency Normalization and Self-Adaptive Scheme

Before deriving our new formulation, we start by investigating the influence of the different quasi-Helmholtz components of $\boldsymbol{j}$ on the scattered or radiated near and far fields.

A. Relevant Current Components

To assess the influence of a current component on the far field (FF), we utilize the stabilized evaluation [28]

$$\begin{aligned}\boldsymbol{e}^{\mathrm{FF}}(\boldsymbol{r}) = &\sum_{n=1}^{N} \left[\boldsymbol{j}_{\mathrm{sol,hsol}}\right]_n \iint_{\Gamma} \boldsymbol{f}_n(\boldsymbol{r}') \,\mathfrak{T}\left(\mathrm{e}^{-\mathrm{j}\boldsymbol{k}\cdot\boldsymbol{r}'} - 1\right) \mathrm{d}S(\boldsymbol{r}') \\ &+ \sum_{n=1}^{N} \left[\boldsymbol{j}_{\mathrm{nsol}}\right]_n \iint_{\Gamma} \boldsymbol{f}_n(\boldsymbol{r}') \,\mathrm{e}^{-\mathrm{j}\boldsymbol{k}\cdot\boldsymbol{r}'} \,\mathrm{d}S(\boldsymbol{r}') \,, \end{aligned} \tag{12}$$

where $\mathfrak{T}(\cdot)$ denotes a Taylor series expansion around $\boldsymbol{k}\cdot\boldsymbol{r} = 0$, and we divided by a normalization factor $-\mathrm{j}k\mathrm{e}^{-\mathrm{j}kr}/(4\pi r)$. Since $\mathfrak{T}(\mathrm{e}^{-\mathrm{j}\boldsymbol{k}\cdot\boldsymbol{r}} - 1) = O(k)$, the combined current component $\boldsymbol{j}_{\mathrm{sol,hsol}}$ is scaled with an additional factor k. Adopting the notation $O(k^a) < O(k^b) \Leftrightarrow a < b$, we consider $\boldsymbol{j}_{\mathrm{sol,hsol}}$ relevant for the far-field computation if $O(k\boldsymbol{j}_{\mathrm{sol,hsol}}) \leq O(\boldsymbol{j}_{\mathrm{nsol}})$. Likewise, $\boldsymbol{j}_{\mathrm{nsol}}$ is relevant for the far-field computation if $O(\boldsymbol{j}_{\mathrm{nsol}}) \leq O(k\boldsymbol{j}_{\mathrm{sol,hsol}})$.

Analogously, we can determine if a current component is relevant for the computation of the electric or the magnetic near field (NF). In the case of the electric NF, we use its stabilized evaluation

$$\begin{aligned}\boldsymbol{e}^{\mathrm{NF}}(\boldsymbol{r}) = -\mathrm{j}\sum_{n=1}^{N} \left[\boldsymbol{j}_{\mathrm{nsol}}\right]_n &\left(k \iint_{\Gamma} G\boldsymbol{f}_n(\boldsymbol{r}') \,\mathrm{d}S(\boldsymbol{r}') \right. \\ &\left. + k^{-1} \iint_{\Gamma} \nabla'\cdot\boldsymbol{f}_n(\boldsymbol{r}')\nabla G \,\mathrm{d}S(\boldsymbol{r}') \right) \\ &- \mathrm{j}k \sum_{n=1}^{N} \left[\boldsymbol{j}_{\mathrm{sol,hsol}}\right]_n \iint_{\Gamma} G\boldsymbol{f}_n(\boldsymbol{r}') \,\mathrm{d}S(\boldsymbol{r}') \,, \end{aligned} \tag{13}$$

which introduces a scaling of $\boldsymbol{j}_{\mathrm{sol,hsol}}$ with k and of $\boldsymbol{j}_{\mathrm{nsol}}$ with $1/k$. In the case of the magnetic NF evaluation, both current components are weighed identically.

As an example, consider a plane-wave excitation, where we have $\|\boldsymbol{j}_{\mathrm{sol,hsol}}\| = O(1)$ and $\|\boldsymbol{j}_{\mathrm{nsol}}\| = O(k)$: here, only $\boldsymbol{j}_{\mathrm{nsol}}$ is relevant for the electric NF, only $\boldsymbol{j}_{\mathrm{sol,hsol}}$ is relevant for the magnetic NF, but both current components are relevant for the FF. Analogously, the relevant current components that are required to recover the NFs and the FF can be derived for the excitations shown in Table II, where we used the physical current scalings given in [5], [29]. In addition, we have included the cases of the spherical TE_{mn} and TM_{mn} modes (corresponding to the definitions in [30, pp. 325ff] with $n \in \{1, 2, \dots\}$ and $|m| \leq n$) based on the physically correct scalings of the current components $\|\boldsymbol{j}_{\mathrm{TE,sol,hsol}}\| = O(k^{-(n+1)})$ and $\|\boldsymbol{j}_{\mathrm{TE,nsol}}\| = O(k^{-(n-1)})$ for TE modes as well as $\|\boldsymbol{j}_{\mathrm{TM,sol,hsol}}\| = O(k^{-n})$ and $\|\boldsymbol{j}_{\mathrm{TM,nsol}}\| = O(k^{-n})$ for TM modes. The asymptotic scalings can be derived from the RHS component scalings given in [10] and a Schur complement analysis of $\boldsymbol{j}'' = \boldsymbol{T}^{-1}_{\Lambda H\Sigma}\boldsymbol{Q}^{\mathrm{T}}\boldsymbol{e}^{\mathrm{ex}}$ (see also the following sections).

Table II
RELEVANT CURRENT COMPONENTS REQUIRED TO RECOVER NFS AND FF FOR $k \to 0$.

	plane wave	Hertzian dipole	el. ring current	mag. dipole	mag. ring current	ind. gap	cap. gap	TE$_{mn}$	TM$_{mn}$
e-NF	$\boldsymbol{j}_{\text{nsol}}$	$\boldsymbol{j}_{\text{nsol}}$	$\boldsymbol{j}_{\text{sol,hsol}}$, $\boldsymbol{j}_{\text{nsol}}$	$\boldsymbol{j}_{\text{sol,hsol}}$, $\boldsymbol{j}_{\text{nsol}}$	$\boldsymbol{j}_{\text{nsol}}$	$\boldsymbol{j}_{\text{sol,hsol}}$, $\boldsymbol{j}_{\text{nsol}}$	$\boldsymbol{j}_{\text{nsol}}$	$\boldsymbol{j}_{\text{sol,hsol}}$, $\boldsymbol{j}_{\text{nsol}}$	$\boldsymbol{j}_{\text{nsol}}$
h-NF	$\boldsymbol{j}_{\text{sol,hsol}}$	$\boldsymbol{j}_{\text{sol,hsol}}$, $\boldsymbol{j}_{\text{nsol}}$	$\boldsymbol{j}_{\text{sol,hsol}}$	$\boldsymbol{j}_{\text{sol,hsol}}$	$\boldsymbol{j}_{\text{sol,hsol}}$, $\boldsymbol{j}_{\text{nsol}}$	$\boldsymbol{j}_{\text{sol,hsol}}$	$\boldsymbol{j}_{\text{sol,hsol}}$, $\boldsymbol{j}_{\text{nsol}}$	$\boldsymbol{j}_{\text{sol,hsol}}$	$\boldsymbol{j}_{\text{sol,hsol}}$, $\boldsymbol{j}_{\text{nsol}}$
FF	$\boldsymbol{j}_{\text{sol,hsol}}$, $\boldsymbol{j}_{\text{nsol}}$	$\boldsymbol{j}_{\text{nsol}}$	$\boldsymbol{j}_{\text{sol,hsol}}$	$\boldsymbol{j}_{\text{sol,hsol}}$	$\boldsymbol{j}_{\text{nsol}}$	$\boldsymbol{j}_{\text{sol,hsol}}$	$\boldsymbol{j}_{\text{nsol}}$	$\boldsymbol{j}_{\text{sol,hsol}}$	$\boldsymbol{j}_{\text{nsol}}$

Clearly, for all of the excitations in Table II, both $\boldsymbol{j}_{\text{nsol}}$ and $\boldsymbol{j}_{\text{sol,hsol}}$ must be recovered accurately if one desires to compute both FF and NFs accurately. Even more, both current components have to be recovered with a similar relative accuracy as one component can solely determine the accuracy of a field even though its magnitude might be small compared to the other current component. To ensure accurate recovery, we study, in a first step, the frequency scalings of the loop-star decomposed system (6).

B. Self-Adaptive Normalization for Loop-Star Basis

As will be shown in the following, while for a plane-wave excitation the normalization matrices in (6) can be chosen as $\boldsymbol{D}_1 = \boldsymbol{D}_2 = (1, 1, k)$ [2], $\boldsymbol{D}_1 = \boldsymbol{D}_2 = \text{diag}(1/\sqrt{k}, 1/\sqrt{k}, \sqrt{k})$ [5], or $\boldsymbol{D}_1 = \text{diag}(1/k, 1/k, 1)$ and $\boldsymbol{D}_2 = \text{diag}(1, 1, k)$ [19], for arbitrary excitations this yields, in general, wrong solutions; instead, a more flexible approach is required. For the analysis, we use $\boldsymbol{D}_i$ from (7), which allows for an asymmetric normalization. Performing a Schur-complement analysis for the inverse of $\boldsymbol{D}_1\boldsymbol{T}_{\boldsymbol{\Lambda H \Sigma}}\boldsymbol{D}_2$ for $k \to 0$, we obtain

$$\begin{bmatrix} O\left(\|\boldsymbol{j}'_{\text{sol}}\|\right) \\ O\left(\|\boldsymbol{j}'_{\text{hsol}}\|\right) \\ O\left(\|\boldsymbol{j}'_{\text{nsol}}\|\right) \end{bmatrix} = (\boldsymbol{D}_1\boldsymbol{T}_{\boldsymbol{\Lambda H \Sigma}}\boldsymbol{D}_2)^{-1} \begin{bmatrix} O(\alpha_1 \|\boldsymbol{e}_{\text{sol}}\|) \\ O(\gamma_1 \|\boldsymbol{e}_{\text{hsol}}\|) \\ O(\beta_1 \|\boldsymbol{e}_{\text{nsol}}\|) \end{bmatrix}, \tag{14}$$

where we note that $O(\|\boldsymbol{j}'_{\text{sol}}\|) = O(\|\boldsymbol{j}_{\boldsymbol{\Lambda}}\|)$, $O(\|\boldsymbol{j}'_{\text{hsol}}\|) = O(\|\boldsymbol{j}_{\boldsymbol{H}}\|)$, as well as $O(\|\boldsymbol{j}'_{\text{nsol}}\|) = O(\|\boldsymbol{j}_{\boldsymbol{\Sigma}}\|)$ since the multiplication with the mapping matrices $\boldsymbol{\Lambda}$, $\boldsymbol{H}$, and $\boldsymbol{\Sigma}$ does not change the scaling in k. The blocks of the matrix $(\boldsymbol{D}_1\boldsymbol{T}_{\boldsymbol{\Lambda H \Sigma}}\boldsymbol{D}_2)^{-1}$ exhibit the scaling

$$\begin{bmatrix} O\left(1/(\alpha_1\alpha_2 k)\right) & O\left(1/(\gamma_1\alpha_2 k)\right) & O\left(k/(\beta_1\alpha_2)\right) \\ O\left(1/(\alpha_1\gamma_2 k)\right) & O\left(1/(\gamma_1\gamma_2 k)\right) & O\left(k/(\beta_1\gamma_2)\right) \\ O\left(k/(\alpha_1\beta_2)\right) & O\left(k/(\gamma_1\beta_2)\right) & O\left(k/(\beta_1\beta_2)\right) \end{bmatrix}, \tag{15}$$

which is a direct generalization of the findings in [29]. In order to obtain a well-conditioned matrix for $k \to 0$, we enforce that the blocks on the main diagonal scale as $O(1)$; thus, the coefficients must obey

$$\alpha_1\alpha_2 = O(1/k), \quad \gamma_1\gamma_2 = O(1/k), \tag{16}$$

and

$$\beta_1\beta_2 = O(k). \tag{17}$$

Inserting (16) and (17) into (15) and forming the matrix-vector product in (14) results in

$$\begin{bmatrix} O\left(\|\boldsymbol{j}'_{\text{sol}}\|\right) \\ O\left(\|\boldsymbol{j}'_{\text{hsol}}\|\right) \\ O\left(\|\boldsymbol{j}'_{\text{nsol}}\|\right) \end{bmatrix} = \begin{bmatrix} O\left(\alpha_1 \|\boldsymbol{e}_{\text{sol}}\| + \alpha_1 \|\boldsymbol{e}_{\text{hsol}}\| + \alpha_1 k^2 \|\boldsymbol{e}_{\text{nsol}}\|\right) \\ O\left(\gamma_1 \|\boldsymbol{e}_{\text{sol}}\| + \gamma_1 \|\boldsymbol{e}_{\text{hsol}}\| + \gamma_1 k^2 \|\boldsymbol{e}_{\text{nsol}}\|\right) \\ O\left(\beta_1 \|\boldsymbol{e}_{\text{nsol}}\| + \beta_1 \|\boldsymbol{e}_{\text{sol}}\| + \beta_1 \|\boldsymbol{e}_{\text{hsol}}\|\right) \end{bmatrix}, \tag{18}$$

which shows that, dependant on the scalings of the incident field, the Helmholtz components of $\boldsymbol{j}'$ will differ in their asymptotic behavior in k.

While the standard choices $\alpha_1 = \alpha_2 = \gamma_1 = \gamma_2 = 1/\sqrt{k}$ and $\beta_1 = \beta_2 = \sqrt{k}$ [5] or alternatively $\alpha_1 = \gamma_1 = 1/k$, $\beta_1 = \alpha_2 = \gamma_2 = 1$, and $\beta_2 = k$ [19] satisfy (16) and (17), the resulting quasi-Helmholtz components of $\boldsymbol{j}'$ will, in general, not have the same asymptotic scaling. Consequently, a large relative error in one of the Helmholtz components remains undetected if, for example, the relative residual error of $\boldsymbol{D}_1\boldsymbol{Q}^{\text{T}}\boldsymbol{e}^{\text{ex}} - \boldsymbol{D}_1\boldsymbol{T}_{\boldsymbol{\Lambda H \Sigma}}\boldsymbol{D}_2\boldsymbol{j}'$ is studied (as done by typical iterative solvers for the LSE). As noted, however, in Section III-A, all current components must be recovered with a similar relative accuracy when solving (6) in order to accurately compute all fields. These considerations lead us to impose a second requirement on α_i, γ_i, and β_i: all current components should scale identically, where we, due to the constraints of finite-precision arithmetic, opt for an $O(1)$-type of scaling.

With the aim of satisfying this additional requirement, we first note that the scalings derived in (18) show that the solenoidal components associated with the local and the ones associated with the global loops can be treated identically. Consequently, in all of the following, we set

$$\gamma_i = \alpha_i, \tag{19}$$

and define

$$\|\boldsymbol{e}_{\text{sol,hsol}}\| = \sqrt{\|\boldsymbol{e}_{\text{sol}}\|^2 + \|\boldsymbol{e}_{\text{hsol}}\|^2}. \tag{20}$$

Moreover, we introduce the ratio of the norms of the solenoidal components over the non-solenoidal component

$$w = \|\boldsymbol{e}_{\text{sol,hsol}}\| / \|\boldsymbol{e}_{\text{nsol}}\|. \tag{21}$$

Excluding the trivial case $\|\boldsymbol{e}_{\text{sol,hsol}}\| = \|\boldsymbol{e}_{\text{nsol}}\| = 0$, the scalings in (18) then dictate

$$\alpha_1 = \begin{cases} 1/\|\boldsymbol{e}_{\text{sol,hsol}}\| & \text{for } w \leq O(k^2) \\ 1/(k^2 \|\boldsymbol{e}_{\text{nsol}}\|) & \text{for } w > O(k^2) \end{cases} \tag{22}$$

and

$$\beta_1 = \begin{cases} 1/\|\boldsymbol{e}_{\text{nsol}}\| & \text{for } w \geq O(1) \\ 1/\|\boldsymbol{e}_{\text{sol,hsol}}\| & \text{for } w < O(1) \end{cases}. \tag{23}$$

Note that the case $w > O(k^2)$ includes $\|\boldsymbol{e}_{\text{sol,hsol}}\| = 0$ when interpreting it as the result of $w \to 0$ and the case $w < O(1)$ includes the case $\|\boldsymbol{e}_{\text{nsol}}\| = 0$ when interpreting it as the result of $w \to \infty$. Moreover, definition (20) covers also the cases where $O(\|\boldsymbol{e}_{\text{sol}}\|) \neq O(\|\boldsymbol{e}_{\text{hsol}}\|)$ including the cases where not both but either $\boldsymbol{e}_{\text{sol}}$ or $\boldsymbol{e}_{\text{hsol}}$ vanishes (e.g., as encountered for gap excitations).

Together with (16) and (17) for the remaining coefficients, we find

$$\alpha_2 = 1/(k\alpha_1) \quad \text{and} \quad \beta_2 = k/\beta_1\,, \tag{24}$$

arriving at a scheme that adapts itself to the incident field based on the norms of the RHS components. Hence, there is no need to have *a-priori* information about the nature of the incident field.

C. Quasi-Helmholtz Projector Normalization Factors

When employing the quasi-Helmholtz projector stabilized system (10) instead of the loop-star decomposition, the very same normalization factors (22)-(24) can be employed[3] with the corresponding definitions for $\boldsymbol{e}_{\text{sol,hsol}}$ and $\boldsymbol{e}_{\text{nsol}}$. This follows from the intrinsic relation to the loop-star decomposition, that is, $\boldsymbol{P}_1\boldsymbol{T}\boldsymbol{P}_2 = \boldsymbol{Q}\boldsymbol{N}\boldsymbol{D}_1\boldsymbol{T}_{\Lambda H\Sigma}\boldsymbol{D}_2\boldsymbol{N}\boldsymbol{Q}^{\mathrm{T}}$ with $\boldsymbol{N} = \operatorname{diag}((\boldsymbol{\Lambda}^{\mathrm{T}}\boldsymbol{\Lambda})^{+}, (\boldsymbol{H}^{\mathrm{T}}\boldsymbol{H})^{+}, (\boldsymbol{\Sigma}^{\mathrm{T}}\boldsymbol{\Sigma})^{+})$. However, it should be verified that α_i and β_i in (9) properly take care of another aspect only relevant for the projectors: since solenoidal and non-solenoidal components are stored in the same vector, that is, $\boldsymbol{j}' = \boldsymbol{j}'_{\text{sol,hsol}} + \boldsymbol{j}'_{\text{nsol}}$ and $\boldsymbol{P}_1\boldsymbol{e}^{\text{ex}} = \boldsymbol{e}'_{\text{sol,hsol}} + \boldsymbol{e}'_{\text{nsol}}$, significant digits can be lost if the asymptotic scaling in k of $\boldsymbol{j}'_{\text{sol,hsol}}$ and $\boldsymbol{j}'_{\text{nsol}}$ (or $\boldsymbol{e}'_{\text{sol,hsol}}$ and $\boldsymbol{e}'_{\text{nsol}}$) is different. This is precisely the reason why an imaginary constant was included in the definition of the projectors in [5], where $\boldsymbol{P}_1 = \boldsymbol{P}_2 = \boldsymbol{P}_{\Lambda H}/\sqrt{k} + \mathrm{j}\sqrt{k}\boldsymbol{P}_{\Sigma}$ was employed. Due to the imaginary constant, for example, for the inductive gap excitation the dominant contribution of $\boldsymbol{j}'_{\text{sol,hsol}}$ was stored in the imaginary part and the dominant contribution of $\boldsymbol{j}'_{\text{nsol}}$ in the real part of $\boldsymbol{j}'$, where we consider a component as dominant if its asymptotic behavior $O(k^a) < O(k^b)$ with k^b as the scaling for the other component.[4] This approach relies on the circumstance that real and imaginary part of each quasi-Helmholtz component often exhibit a different asymptotic scaling, so that, in fact, only one of the parts is relevant for an accurate field computation in low-frequency scenarios. However, using the factors α_i and β_i as defined in (22)-(24) for $\boldsymbol{P}_i$, the inclusion of an imaginary constant is in the first place no longer necessary.

In order to illustrate this problem of the significant digits in more detail, we consider the physical frequency scalings of the RHS for seven different types of excitations. Those can be derived as shown in Appendix A, where the findings of [29] are generalized, resulting in the first three rows of Table III. Note that in contrast to the analysis so far, we study now real and imaginary part separately to show that indeed no dominant contribution is lost. The scalings show that directly storing the components in one vector would lead to a loss of significant digits for a Hertzian dipole or a magnetic ring current excitation, since the solenoidal components scale differently than the non-solenoidal components. The next three rows show the scalings using the standard normalization from [5]. Here the real and the imaginary part of the non-solenoidal components are interchanged, which allows to store the components in one vector for all the considered excitations. However, for the excitation by spherical TE and TM modes, this approach fails as shown by Table IV. Both, real and imaginary part have the same asymptotic scaling such that none can be neglected. At the same time, the here proposed normalization shown in the last rows (of Table III and Table IV) works independently of the specific scalings of the RHS and without introducing an imaginary constant, since it does not rely on storing one dominant component in the real and the other in the imaginary part: each dominant component is normalized to scale as $O(1)$, and thus, they can be added without the danger of losing significant digits.

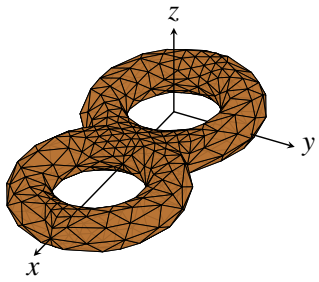

Fig. 1. Double torus with $N_H = 4$ global loops: each torus with outer radius 1 m and inner radius 0.5 m. Second torus at $x = 1.55$ m. Discretized by 848 triangles and 1272 RWGs.

To complete the picture, we study also the scalings of the solution current components in Table V: the first three rows show the physical scalings as obtained by separately handling real and imaginary part in (14). Evidently, storing the physical current components in one vector fails for the electric ring current, the magnetic (Fitzgerald) dipole, and the inductive gap excitation. From $\boldsymbol{j} = \boldsymbol{j}_{\text{sol,hsol}} + \boldsymbol{j}_{\text{nsol}} = \boldsymbol{P}_2\boldsymbol{j}' = \alpha_2\boldsymbol{j}'_{\text{sol,hsol}} + \beta_2\boldsymbol{j}'_{\text{nsol}}$, it can be seen that the solution current of the preconditioned LSE scales as

$$\boldsymbol{j}'_{\text{sol,hsol}} = \boldsymbol{j}_{\text{sol,hsol}}/\alpha_2 \qquad \text{and} \qquad \boldsymbol{j}'_{\text{nsol}} = \boldsymbol{j}_{\text{nsol}}/\beta_2\,. \tag{25}$$

Using the normalization from [5], rows two to six in Table V show that, at least for the considered excitations, all current components can be stored in one vector. However, again for the TE_{mn} and TM_{mn} modes this fails as, for example, $\|\boldsymbol{j}_{\text{TE,sol,hsol}}\|_\star = O(k^{-(n+1)}) + \mathrm{j}O(k^{-(n+1)})$ and $\|\boldsymbol{j}_{\text{TE,nsol}}\|_\star = O(k^{-(n-1)}) + \mathrm{j}O(k^{-(n-1)})$. Even more, for all the excitations (except for the plane wave) the dominant components of the current still scale differently, hinting that they cannot be recovered with a similar relative accuracy in a straightforward manner but an ad-hoc technique is required. This can be avoided when the proposed normalization scheme is employed as shown in the last three rows.

As an example of which current components can be recovered, we consider the double torus in Fig. 1 excited by a magnetic diople. Real and imaginary part of the determined current components are depicted in Fig. 2 (a) for the standard

[3]Note that due to (19) there is no need to split $\boldsymbol{P}_{\Lambda H}$ into $\boldsymbol{P}_{\Lambda}$ and $\boldsymbol{P}_H$.

[4]For the actual recovery of the relevant current components, the normalization of [5] of course requires an ad-hoc technique, which is avoided by the here proposed approach.

Table III
SCALING OF REAL AND IMAGINARY PART OF THE RHS COMPONENTS FOR $k \to 0$ WITH $\|a\|_\star = \|\mathrm{Re}\{a\}\| + \mathrm{j}\|\mathrm{Im}\{a\}\|$.

	plane wave	Hertzian dipole	el. ring current	mag. dipole	mag. ring current	ind. gap	cap. gap
$\|e_{\mathrm{sol}}\|_\star$	$O(k^2)+\mathrm{j}O(k)$	$O(k^4)+\mathrm{j}O(k)$	$O(k^4)+\mathrm{j}O(k)$	$O(1)+\mathrm{j}O(k^3)$	$O(k^2)+\mathrm{j}O(k^5)$	$0+\mathrm{j}0$	$0+\mathrm{j}0$
$\|e_{\mathrm{hsol}}\|_\star$	$O(k^2)+\mathrm{j}O(k)$	$O(k^4)+\mathrm{j}O(k)$	$O(k^4)+\mathrm{j}O(k)$	$O(1)+\mathrm{j}O(k^3)$	$O(k^2)+\mathrm{j}O(k^5)$	$O(1)+\mathrm{j}0$	$0+\mathrm{j}0$
$\|e_{\mathrm{nsol}}\|_\star$	$O(1)+\mathrm{j}O(k)$	$O(k^2)+\mathrm{j}O(1/k)$	$O(k^4)+\mathrm{j}O(k)$	$O(1)+\mathrm{j}O(k^3)$	$O(1)+\mathrm{j}O(k^3)$	$O(1)+\mathrm{j}0$	$O(1)+\mathrm{j}0$
$1/\sqrt{k}\|e_{\mathrm{sol}}\|_\star$	$O(k^{3/2})+\mathrm{j}O(k^{1/2})$	$O(k^{7/2})+\mathrm{j}O(k^{1/2})$	$O(k^{7/2})+\mathrm{j}O(k^{1/2})$	$O(k^{-1/2})+\mathrm{j}O(k^{5/2})$	$O(k^{3/2})+\mathrm{j}O(k^{9/2})$	$0+\mathrm{j}0$	$0+\mathrm{j}0$
$1/\sqrt{k}\|e_{\mathrm{hsol}}\|_\star$	$O(k^{3/2})+\mathrm{j}O(k^{1/2})$	$O(k^{7/2})+\mathrm{j}O(k^{1/2})$	$O(k^{7/2})+\mathrm{j}O(k^{1/2})$	$O(k^{-1/2})+\mathrm{j}O(k^{5/2})$	$O(k^{3/2})+\mathrm{j}O(k^{9/2})$	$O(k^{-1/2})+\mathrm{j}0$	$0+\mathrm{j}0$
$\mathrm{j}\sqrt{k}\|e_{\mathrm{nsol}}\|_\star$	$O(k^{3/2})+\mathrm{j}O(k^{1/2})$	$O(k^{-1/2})+\mathrm{j}O(k^{5/2})$	$O(k^{3/2})+\mathrm{j}O(k^{9/2})$	$O(k^{7/2})+\mathrm{j}O(k^{1/2})$	$O(k^{7/2})+\mathrm{j}O(k^{1/2})$	$0+\mathrm{j}O(k^{1/2})$	$0+\mathrm{j}O(k^{1/2})$
$\alpha_1\|e_{\mathrm{sol}}\|_\star$	$O(k)+\mathrm{j}O(1)$	$O(k^3)+\mathrm{j}O(1)$	$O(k^3)+\mathrm{j}O(1)$	$O(1)+\mathrm{j}O(k^3)$	$O(1)+\mathrm{j}O(k^3)$	$0+\mathrm{j}0$	$0+\mathrm{j}0$
$\alpha_1\|e_{\mathrm{hsol}}\|_\star$	$O(k)+\mathrm{j}O(1)$	$O(k^3)+\mathrm{j}O(1)$	$O(k^3)+\mathrm{j}O(1)$	$O(1)+\mathrm{j}O(k^3)$	$O(1)+\mathrm{j}O(k^3)$	$O(1)+\mathrm{j}0$	$0+\mathrm{j}0$
$\beta_1\|e_{\mathrm{nsol}}\|_\star$	$O(1)+\mathrm{j}O(k)$	$O(k^3)+\mathrm{j}O(1)$	$O(k^3)+\mathrm{j}O(1)$	$O(1)+\mathrm{j}O(k^3)$	$O(1)+\mathrm{j}O(k^3)$	$O(1)+\mathrm{j}0$	$O(1)+\mathrm{j}0$

Table IV
SCALING OF REAL AND IMAGINARY PART OF THE RHS COMPONENTS FOR $k \to 0$ WITH $\|a\|_\star = \|\mathrm{Re}\{a\}\| + \mathrm{j}\|\mathrm{Im}\{a\}\|$.

	TE_{mn}	TM_{mn}
$\|e_{\mathrm{sol,hsol}}\|_\star$	$O(k^{-n})+\mathrm{j}O(k^{-n})$	$O(k^{-(n-1)})+\mathrm{j}O(k^{-(n-1)})$
$\|e_{\mathrm{nsol}}\|_\star$	$O(k^{-n})+\mathrm{j}O(k^{-n})$	$O(k^{-(n+1)})+\mathrm{j}O(k^{-(n+1)})$
$1/\sqrt{k}\|e_{\mathrm{sol,hsol}}\|_\star$	$O(k^{-n-1/2})+\mathrm{j}O(k^{-n-1/2})$	$O(k^{-(n-1/2)})+\mathrm{j}O(k^{-(n-1/2)})$
$\mathrm{j}\sqrt{k}\|e_{\mathrm{nsol}}\|_\star$	$O(k^{-n+1/2})+\mathrm{j}O(k^{-n+1/2})$	$O(k^{-(n+1/2)})+\mathrm{j}O(k^{-(n+1/2)})$
$\alpha_1\|e_{\mathrm{sol,hsol}}\|_\star$	$O(1)+\mathrm{j}O(1)$	$O(1)+\mathrm{j}O(1)$
$\beta_1\|e_{\mathrm{nsol}}\|_\star$	$O(1)+\mathrm{j}O(1)$	$O(1)+\mathrm{j}O(1)$

normalization and in Fig. 2 (b) for the proposed normalization. In order to ensure a high accuracy, a direct solver is employed. While the standard normalization, at first glance, seems to approximate the theoretical scalings (indicated by dashed lines) better, only the adaptive normalization maintains the correct scalings of the dominant components for all frequencies. This is, however, the decisive property. The worse agreement of the non-dominant components is not relevant for the resulting fields as the non-dominant components are (in this case 13) orders of magnitude smaller than the dominant components. A similar behavior can be observed for an excitation by an electric ring current as shown in Fig. 2 (c) and (d), which confirms, again, the preceding analysis.

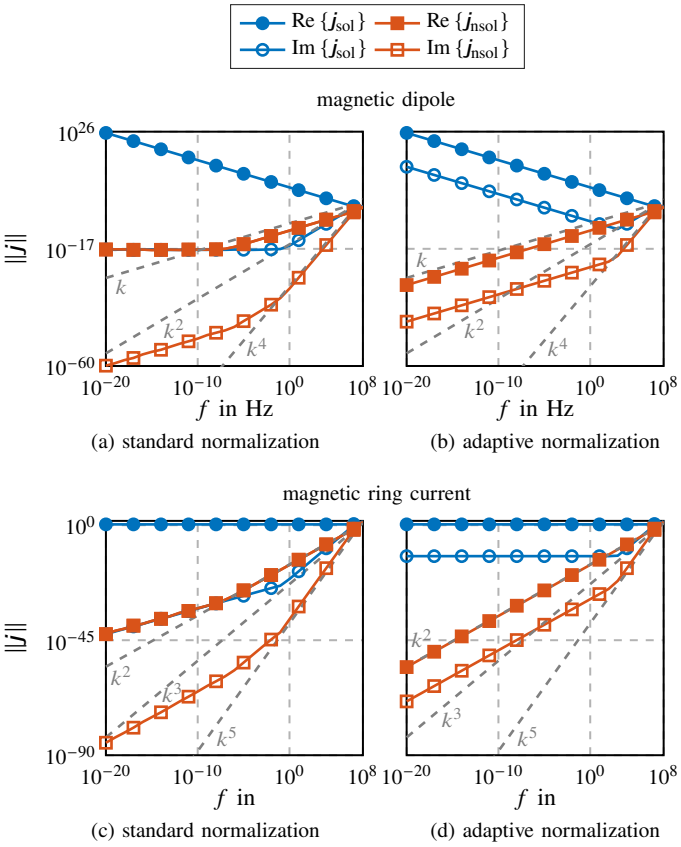

(a) standard normalization (b) adaptive normalization

(c) standard normalization (d) adaptive normalization

Fig. 2. Scaling of real and imaginary part of the recovered current components for a double torus excited by a magnetic dipole and ring current.

IV. EIGENVALUE DISTRIBUTION AND IMPLEMENTATION DETAILS

The definition of the normalization constants α_i and β_i in (22)-(24) allows for two more improvements leading typically to faster convergence of iterative solvers. By reintroducing an imaginary constant j and a constant C (to be defined for the loop-star basis and the quasi-Helmholtz projectors, respectively, in the following subsections), we ultimately propose to choose the normalization factors

$$\alpha_1 = \begin{cases} \sqrt{-\mathrm{j}C}/\|e_{\mathrm{sol,hsol}}\| & \text{for } \|e_{\mathrm{sol,hsol}}\| \neq 0\,, \\ \sqrt{-\mathrm{j}C}/(k^2\,\|e_{\mathrm{nsol}}\|) & \text{for } \|e_{\mathrm{sol,hsol}}\| = 0\,, \end{cases} \tag{26}$$

and

$$\beta_1 = \begin{cases} 1/(\sqrt{-\mathrm{j}C}\|e_{\mathrm{nsol}}\|) & \text{for } \|e_{\mathrm{nsol}}\| \neq 0\,, \\ 1/(\sqrt{-\mathrm{j}C}\,\|e_{\mathrm{sol,hsol}}\|) & \text{for } \|e_{\mathrm{nsol}}\| = 0\,, \end{cases} \tag{27}$$

where the simplified conditions for the case distinctions (not involving w) are sufficient for practical purposes as will be detailed in the following section. Together with (16) and (17), we then find for the remaining coefficients

$$\alpha_2 = C/(\mathrm{j}k\alpha_1) \quad \text{and} \quad \beta_2 = \mathrm{j}k/(C\beta_1)\,, \tag{28}$$

where still (19) is employed for the γ_i in the context of the loop-star decomposition. The motivation for these modifications will again be discussed first for the loop-star decomposition and then for the quasi-Helmholtz projectors.

A. On the Simplification of the Conditions to be Checked

The suggested simplified conditions for the case distinctions in (26) and (27) are based on the observation, that except for

Table V
SCALING OF REAL AND IMAGINARY PART OF THE CURRENT COMPONENTS FOR $k \to 0$ WITH $\|\boldsymbol{a}\|_\star = \|\mathrm{Re}\,\{\boldsymbol{a}\}\| + \mathrm{j}\|\mathrm{Im}\,\{\boldsymbol{a}\}\|$.

	plane wave	Hertzian dipole	el. ring current	mag. dipole	mag. ring current	ind. gap	cap. gap
$\|\boldsymbol{j}_{\mathrm{sol}}\|_\star$	$O(1)+\mathrm{j}O(k)$	$O(1)+\mathrm{j}O(k^3)$	$O(1)+\mathrm{j}O(k^3)$	$O(k^2)+\mathrm{j}O(1/k)$	$O(k^4)+\mathrm{j}O(k)$	$O(k^2)+\mathrm{j}O(1/k)$	$O(k^4)+\mathrm{j}O(k)$
$\|\boldsymbol{j}_{\mathrm{hsol}}\|_\star$	$O(1)+\mathrm{j}O(k)$	$O(1)+\mathrm{j}O(k^3)$	$O(1)+\mathrm{j}O(k^3)$	$O(k^2)+\mathrm{j}O(1/k)$	$O(k^4)+\mathrm{j}O(k)$	$O(k^2)+\mathrm{j}O(1/k)$	$O(k^4)+\mathrm{j}O(k)$
$\|\boldsymbol{j}_{\mathrm{nsol}}\|_\star$	$O(k^2)+\mathrm{j}O(k)$	$O(1)+\mathrm{j}O(k^3)$	$O(k^2)+\mathrm{j}O(k^5)$	$O(k^4)+\mathrm{j}O(k)$	$O(k^4)+\mathrm{j}O(k)$	$O(k^4)+\mathrm{j}O(k)$	$O(k^4)+\mathrm{j}O(k)$
$\|\boldsymbol{j}_{\mathrm{sol}}\|_\star\sqrt{k}$	$O(k^{1/2})+\mathrm{j}O(k^{3/2})$	$O(k^{1/2})+\mathrm{j}O(k^{7/2})$	$O(k^{1/2})+\mathrm{j}O(k^{7/2})$	$O(k^{5/2})+\mathrm{j}O(k^{-1/2})$	$O(k^{9/2})+\mathrm{j}O(k^{3/2})$	$O(k^{5/2})+\mathrm{j}O(k^{-1/2})$	$O(k^{9/2})+\mathrm{j}O(k^{3/2})$
$\|\boldsymbol{j}_{\mathrm{hsol}}\|_\star\sqrt{k}$	$O(k^{1/2})+\mathrm{j}O(k^{3/2})$	$O(k^{1/2})+\mathrm{j}O(k^{7/2})$	$O(k^{1/2})+\mathrm{j}O(k^{7/2})$	$O(k^{5/2})+\mathrm{j}O(k^{-1/2})$	$O(k^{9/2})+\mathrm{j}O(k^{3/2})$	$O(k^{5/2})+\mathrm{j}O(k^{-1/2})$	$O(k^{9/2})+\mathrm{j}O(k^{3/2})$
$\|\boldsymbol{j}_{\mathrm{nsol}}\|_\star\mathrm{j}/\sqrt{k}$	$O(k^{1/2})+\mathrm{j}O(k^{3/2})$	$O(k^{5/2})+\mathrm{j}O(k^{-1/2})$	$O(k^{9/2})+\mathrm{j}O(k^{3/2})$	$O(k^{1/2})+\mathrm{j}O(k^{7/2})$	$O(k^{1/2})+\mathrm{j}O(k^{7/2})$	$O(k^{1/2})+\mathrm{j}O(k^{7/2})$	$O(k^{1/2})+\mathrm{j}O(k^{7/2})$
$\|\boldsymbol{j}_{\mathrm{sol}}\|_\star/\alpha_2$	$O(1)+\mathrm{j}O(k)$	$O(1)+\mathrm{j}O(k^3)$	$O(1)+\mathrm{j}O(k^3)$	$O(k^3)+\mathrm{j}O(1)$	$O(k^3)+\mathrm{j}O(1)$	$O(k^3)+\mathrm{j}O(1)$	$O(k^3)+\mathrm{j}O(1)$
$\|\boldsymbol{j}_{\mathrm{hsol}}\|_\star/\alpha_2$	$O(1)+\mathrm{j}O(k)$	$O(1)+\mathrm{j}O(k^3)$	$O(1)+\mathrm{j}O(k^3)$	$O(k^3)+\mathrm{j}O(1)$	$O(k^3)+\mathrm{j}O(1)$	$O(k^3)+\mathrm{j}O(1)$	$O(k^3)+\mathrm{j}O(1)$
$\|\boldsymbol{j}_{\mathrm{nsol}}\|_\star/\beta_2$	$O(k)+\mathrm{j}O(1)$	$O(1)+\mathrm{j}O(k^3)$	$O(1)+\mathrm{j}O(k^3)$	$O(k^3)+\mathrm{j}O(1)$	$O(k^3)+\mathrm{j}O(1)$	$O(k^3)+\mathrm{j}O(1)$	$O(k^3)+\mathrm{j}O(1)$

the capacitive gap excitation for all standard excitations listed in Table III, the ratio in (21) satisfies

$$O(1) \le w \le O(k^2) \tag{29}$$

as can be seen from the first three rows. The capacitive gap excitation, on the other hand, is accounted for by the case $\|\boldsymbol{e}_{\mathrm{sol,hsol}}\| = 0$. Even when combining arbitrary TE_{mn} and TM_{mn} modes with arbitrary orders n, the relation (29) is satisfied with the sole exception when Γ is a sphere placed in the origin, all shown in Appendix B. In this particular case, $\|\boldsymbol{e}_{\mathrm{TM,sol}}\| = 0$. Consequently, if no other excitations than the ones listed are present, the case distinctions only require to check whether one of the norms is zero. For cases not covered by (29), the more general conditions on w given in (22) and (23) can be checked by evaluating the norms at least at two frequencies.

B. Loop-Star Decomposition

The idea of introducing the constant C in (26) and (27) is to improve the overall condition number of the system matrix. Choosing it similar to the one suggested in [28] as

$$C = \sqrt{\frac{k\|\boldsymbol{\Sigma}^{\mathrm{T}}\boldsymbol{T}\boldsymbol{\Sigma}\|}{\|[\boldsymbol{\Lambda}\ \boldsymbol{H}]^{\mathrm{T}}\boldsymbol{T}_{\mathrm{A}}[\boldsymbol{\Lambda}\ \boldsymbol{H}]\|}} \tag{30}$$

enforces an equal contribution of the scalar and the vector potential. The matrix norms in this expression can be determined efficiently as $\|\boldsymbol{\Upsilon}\| = \sqrt{\lambda_{\max}(\boldsymbol{\Upsilon}^{\mathrm{H}}\boldsymbol{\Upsilon})}$ for a square matrix $\boldsymbol{\Upsilon}$ with $\lambda_{\max}(\boldsymbol{\Upsilon}^{\mathrm{H}}\boldsymbol{\Upsilon})$ denoting the largest eigenvalue of $\boldsymbol{\Upsilon}^{\mathrm{H}}\boldsymbol{\Upsilon}$. This eigenvalue can be estimated, for example, via a few Arnoldi iterations or the power iteration method (which are both compatible with matrix-free methods) [31], [32].

The factor j, on the other hand, causes $\boldsymbol{D}_1\boldsymbol{T}_{\boldsymbol{\Lambda H\Sigma}}\boldsymbol{D}_2$ to have only positive eigenvalues in the static limit: For $O(1) \le w \le O(k^2)$, the matrix $\boldsymbol{D}_1\boldsymbol{T}_{\boldsymbol{\Lambda H\Sigma}}\boldsymbol{D}_2$ exhibits the block structure

$$\begin{bmatrix} \boldsymbol{A}_{N_{\Lambda H}\times N_{\Lambda H}} & \boldsymbol{B}_{N_{\Lambda H}\times N_\Sigma} \\ \boldsymbol{C}_{N_\Sigma\times N_{\Lambda H}} & \boldsymbol{D}_{N_\Sigma\times N_\Sigma} \end{bmatrix} = \begin{bmatrix} O(1) & O(k^2/w) \\ O(w) & O(1) \end{bmatrix}, \tag{31}$$

with $N_{\Lambda H} = N_\Lambda + N_H$ and where

$$w = O(k^\nu)\,. \tag{32}$$

In order for $\boldsymbol{C}$ not to vanish in the static limit, $\nu \le 0$ has to hold. For $\boldsymbol{B}$ not to vanish, on the other hand, $\nu \ge 2$ has to hold. Since both conditions cannot be satisfied at the same time, either $\boldsymbol{C}$ or $\boldsymbol{B}$ or both vanish for $k \to 0$ independent of the RHS. For the case $w > O(k^2)$, we find $\boldsymbol{B} = O(1)$ and $\boldsymbol{C} = O(k^2)$, and for the case $w < O(1)$, we find $\boldsymbol{B} = O(k^2)$ and $\boldsymbol{C} = O(1)$. Thus, for all possible excitation scalings, $\boldsymbol{D}_1\boldsymbol{T}_{\boldsymbol{\Lambda H\Sigma}}\boldsymbol{D}_2$ is at least block triangular (if not block diagonal). In consequence, for the determinant $\det(\boldsymbol{D}_1\boldsymbol{T}_{\boldsymbol{\Lambda H\Sigma}}\boldsymbol{D}_2) = \det(\boldsymbol{A})\det(\boldsymbol{D})$ holds, which shows that the eigenvalues are solely determined by $\boldsymbol{A}$ and $\boldsymbol{D}$. As $\boldsymbol{A}$ and $\boldsymbol{D}$ are known to have positive eigenvalues [33], so does $\boldsymbol{D}_1\boldsymbol{T}_{\boldsymbol{\Lambda H\Sigma}}\boldsymbol{D}_2$ (for $k \to 0$). This property is, in general, beneficial as it leads to faster convergence for typical Krylov subspace methods [34, pp. 205ff].

C. Quasi-Helmholtz Projectors

Similarly, for the quasi-Helmholtz projectors, we introduce [28]

$$C = \sqrt{\frac{\|\boldsymbol{T}_\Phi\|}{\|\boldsymbol{P}_{\Lambda H}\boldsymbol{T}_{\mathrm{A}}\boldsymbol{P}_{\Lambda H}\|}} \tag{33}$$

to improve the overall condition number. Since the imaginary constants were demonstrated to be irrelevant for the significant digits in Section III-C (due to the new normalization scheme), imaginary constants can again be placed to improve the eigenvalue distribution. That this leads to a positive eigenvalues in the static limit also for the quasi-Helmholtz projected EFIE, can be shown by using the block triangular nature of $\boldsymbol{D}_1\boldsymbol{T}_{\boldsymbol{\Lambda H\Sigma}}\boldsymbol{D}_2$ for $k \to 0$ as starting point. Defining the matrix $\boldsymbol{G} = [\boldsymbol{\Lambda}(\boldsymbol{\Lambda}^{\mathrm{T}}\boldsymbol{\Lambda})^{-1/2}\ \boldsymbol{H}^{\mathrm{T}}(\boldsymbol{H}^{\mathrm{T}}\boldsymbol{H})^{-1/2}\ \boldsymbol{\Sigma}(\boldsymbol{\Sigma}^{\mathrm{T}}\boldsymbol{\Sigma})^{-1/2}]$ and the matrix $\boldsymbol{G}_i = \boldsymbol{G}\boldsymbol{D}_i$, the matrix $\boldsymbol{G}_1^{\mathrm{T}}\boldsymbol{T}\boldsymbol{G}_2$ is also block triangular with positive eigenvalues. Furthermore, we have $\boldsymbol{P}_1\boldsymbol{T}\boldsymbol{P}_2 = \boldsymbol{G}\boldsymbol{G}_1^{\mathrm{T}}\boldsymbol{T}\boldsymbol{G}_2\boldsymbol{G}^{\mathrm{T}}$, which allows to deduce properties about the eigenvalues λ_i of $\boldsymbol{P}_1\boldsymbol{T}\boldsymbol{P}_2$. Due to the properties of similarity transforms, we have for the eigenvalues $\lambda_i(\boldsymbol{G}\boldsymbol{G}_1^{\mathrm{T}}\boldsymbol{T}\boldsymbol{G}_2\boldsymbol{G}^{\mathrm{T}}) = \lambda_i(\boldsymbol{G}^{\mathrm{T}}\boldsymbol{G}\boldsymbol{G}_1^{\mathrm{T}}\boldsymbol{T}\boldsymbol{G}_2\boldsymbol{G}^{\mathrm{T}}\boldsymbol{G}^{-\mathrm{T}})$ for $i = 1,\ldots,N$. Using $\boldsymbol{G}^{\mathrm{T}}\boldsymbol{G} = \boldsymbol{\mathsf{I}}$ and $\boldsymbol{G}^{\mathrm{T}}\boldsymbol{G}^{-\mathrm{T}} = \boldsymbol{\mathsf{I}}$, we find

$$\lambda_i(\boldsymbol{P}_1\boldsymbol{T}\boldsymbol{P}_2) = \lambda_i(\boldsymbol{G}_1^{\mathrm{T}}\boldsymbol{T}\boldsymbol{G}_2) \qquad \forall i = 1,\ldots,N, \tag{34}$$

from which the positive eigenvalues of $\boldsymbol{P}_1\boldsymbol{T}\boldsymbol{P}_2$ follow for $k \to 0$.

In order to illustrate the impact, the eigenvalues λ_i of the projected matrix $\boldsymbol{P}_1\boldsymbol{T}\boldsymbol{P}_2$ for the example of the double torus in Fig. 1 are shown in Fig. 3. Only if the imaginary constant is included, we have $\mathrm{Re}\,\{\lambda_i\} > 0$ and $\mathrm{Im}\,\{\lambda_i\}$ is close to being zero. If the frequency is decreased further down to the kHz region as

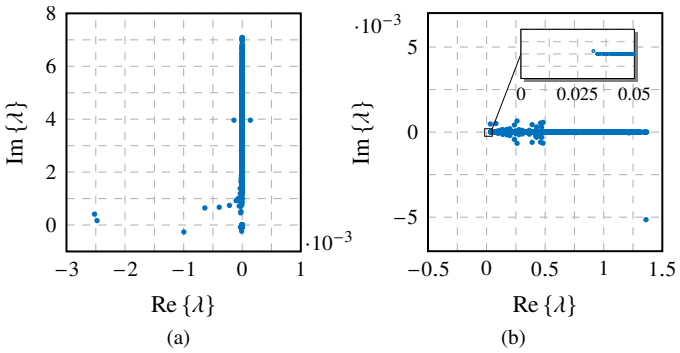

Fig. 3. Eigenvalues λ of the projected matrix of a double torus at 10 MHz (a) without and (b) with imaginary constants.

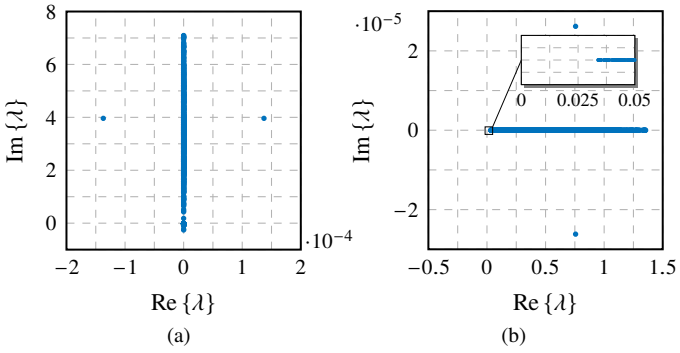

Fig. 4. Eigenvalues λ of the projected matrix of a double torus at 1 kHz (a) without and (b) with imaginary constants.

depicted in Fig. 4, we see that the clustering on the real axis increases further. The influence on the number of iterations for the generalized minimum residual (GMRES) [35], the induced dimension reduction (IDR) [36], and the stabilized bi-conjugate gradient (BiCGstab) [37] algorithm are summarized in Table VI for the case that the double torus is excited by a Hertzian dipole and a relative residual of $\epsilon_{\text{res}} = 1 \times 10^{-6}$ as stopping criterion. Clearly, the iteration count (reflected by the number of matrix-vector products) is reduced if either the imaginary constant or the constant C is included. The best result is obtained if both constants are used simultaneously as is done in the proposed formulation.

V. Numerical Results

To demonstrate the impact of the frequency normalization on the accuracy of the computed scattered and radiated fields, several scenarios are investigated. To this end, we employ the quasi-Helmholtz projectors and compare the standard choice of scaling coefficients, $\alpha_1 = \alpha_2 = \sqrt{C/k}$ and $\beta_1 = \beta_2 = \mathrm{j}\sqrt{k/C}$, where we have included the constant C for a fairer comparison with the adaptive ones in (26) and (27). Again, if not stated otherwise, a GMRES solver is used without restarts and a relative residual of $\epsilon_{\text{res}} = 1 \times 10^{-6}$ as stopping criterion. For the RHS stabilization the approach of [10] is employed and in order to accelerate the computation, an adaptive cross approximation (ACA) algorithm is used [38], [39] with compression rate 1×10^{-4}. The relative worst-case errors

$$\aleph = \max_{\vartheta,\varphi} \left\{ 20 \log \frac{\left| a(\vartheta,\varphi) - \hat{a}(\vartheta,\varphi) \right|}{\max\limits_{\vartheta,\varphi} \left| a(\vartheta,\varphi) \right|} \right\}, \tag{35}$$

Table VI
Number of matrix-vector products for a double torus excited by a Hertzian dipole with and without the inclusion of $\sqrt{\mathrm{j}C}$ in (22) and (23).

solver	f	loop-star				projector			
		none	$\sqrt{\mathrm{j}}$	$\sqrt{C}$	$\sqrt{\mathrm{j}C}$	none	$\sqrt{\mathrm{j}}$	$\sqrt{C}$	$\sqrt{\mathrm{j}C}$
GMRES	10 MHz	945	761	1140	421	206	171	169	43
	1 kHz	945	761	1140	420	206	170	168	43
	1 Hz	945	761	1140	420	206	170	168	43
IDR(8)	10 MHz	7843	1186	2984	498	263	207	213	49
	1 kHz	8895	1119	2829	499	299	198	213	48
	1 Hz	9220	1142	3294	481	301	203	228	50
BiCGstab(2)	10 MHz	-	1272	-	792	488	312	384	52
	1 kHz	-	1272	-	784	476	264	372	48
	1 Hz	-	1272	-	808	508	296	384	52

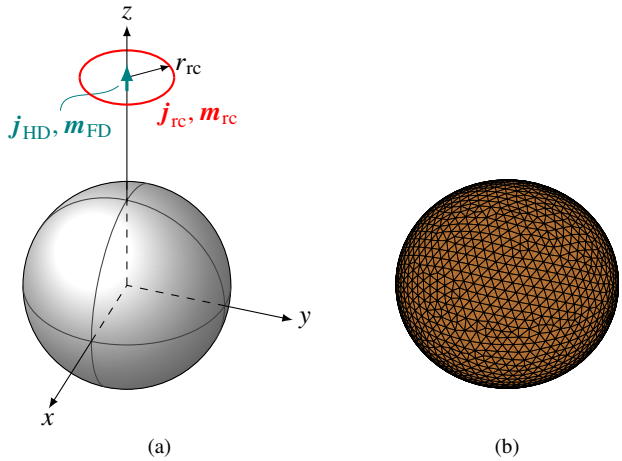

Fig. 5. Scattering from a sphere with radius $r_s = 1$ m (a) excitation with dipoles and ring currents at position $z = 2$ m and radius $r_{\text{rc}} = 0.5$ m; (b) discretized with 3214 triangles and 4821 RWGs.

with $a \in \{e, h, e^{\text{FF}}\}$ are computed based on a spherical 5° grid and NF distances of $r = 8$ m.

A. Scattering from a Sphere

We start with scattering from the sphere shown in Fig. 5, where series expansions are used as reference (see [40, pp. 368 ff.] and [41] for implementation details). The results for different excitations are depicted in Fig. 6. For a plane-wave excitation, the standard normalization is sufficient to determine all fields for the whole frequency range correctly. Figure 6 (b) shows that the adaptive normalization maintains this property. This is as expected: for the plane wave both schemes recover all current components with a similar accuracy.

Considering next the excitation by a Hertzian dipole, Fig. 6 (c) evidences that the adaptive frequency normalization removes an otherwise occurring breakdown in accuracy of the magnetic NF below 1 MHz. That specifically the magnetic NF is affected corresponds well with the preceding analysis (see especially Section III-A): as an incorrect solenoidal current component is recovered, only the magnetic NF is affected in accordance with Table II. Also depicted is the accuracy of an ad-hoc adaption technique using the projectors $\boldsymbol{P} = \boldsymbol{P}_1 = \boldsymbol{P}_2$ from [5] with $\alpha_1 = \alpha_2 = \sqrt{C/k}$ and $\beta_1 = \beta_2 = \mathrm{j}\sqrt{k/C}$. The ad-hoc technique requires that two LSEs are solved. More pre-

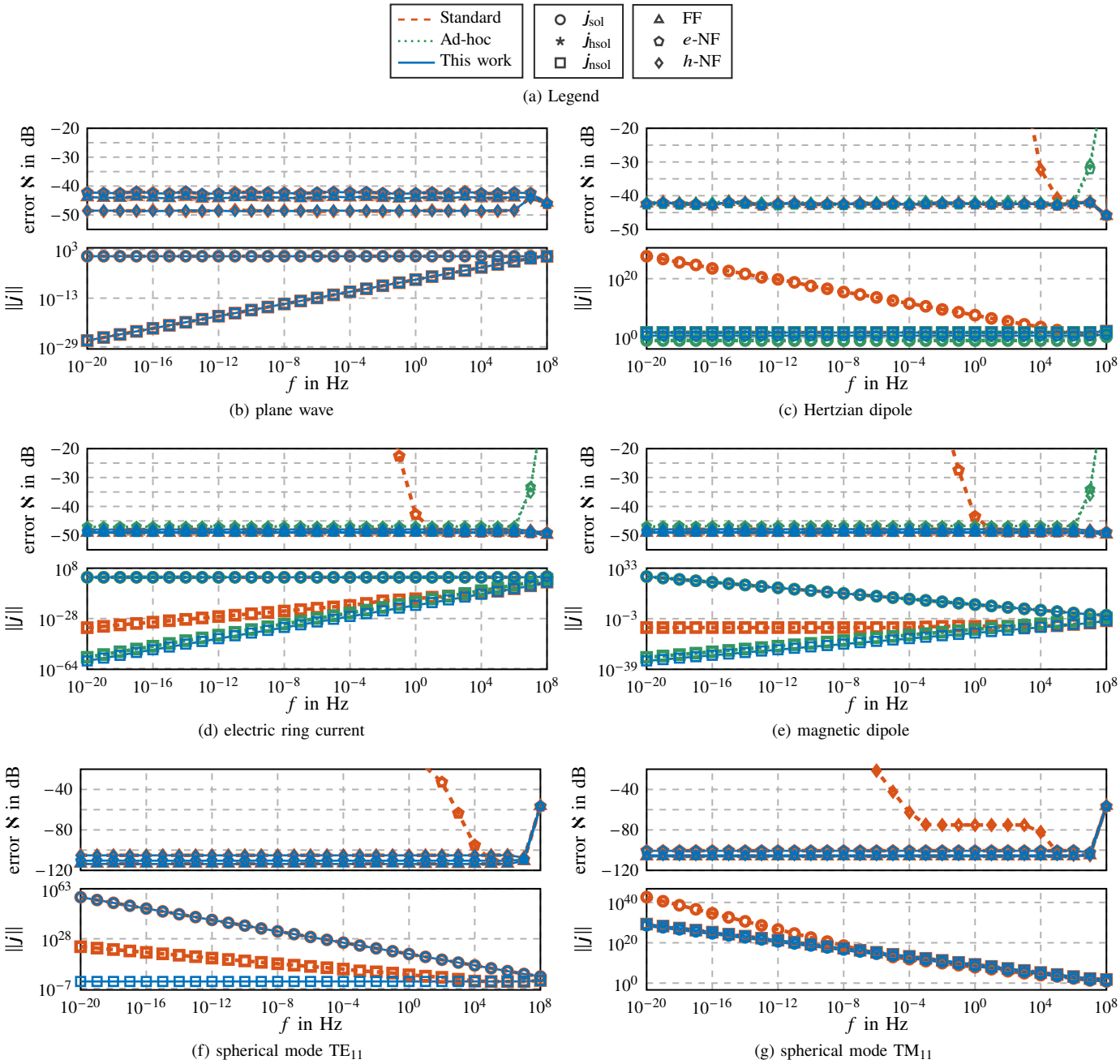

(a) Legend

(b) plane wave

(c) Hertzian dipole

(d) electric ring current

(e) magnetic dipole

(f) spherical mode TE_{11}

(g) spherical mode TM_{11}

Fig. 6. Scattering from a sphere: worst case errors of the FF, the electric, and the magnetic NF, as well as the scaling of the current components.

cisely, as $\|\mathrm{Re}\{\boldsymbol{PTP}\}\| \ll \|\mathrm{Im}\{\boldsymbol{PTP}\}\|$ for low frequencies, the two real valued systems $-\mathrm{Im}\{\boldsymbol{PTP}\}\,\mathrm{Im}\{\boldsymbol{j}'\} = \mathrm{Re}\{\boldsymbol{Pe}^{\mathrm{ex}}\}$ and $\mathrm{Im}\{\boldsymbol{PTP}\}\,\mathrm{Re}\{\boldsymbol{j}'\} = \mathrm{Im}\{\boldsymbol{Pe}^{\mathrm{ex}}\}$ are solved. Depending on the specific dominant components of the excitation (see Table V) only $\mathrm{Re}\{\boldsymbol{j}'\}$ or $\mathrm{Im}\{\boldsymbol{j}'\}$ is used to determine $\boldsymbol{j}_{\mathrm{sol,hsol}}$ and in an analogue fashion to determine $\boldsymbol{j}_{\mathrm{nsol}}$. While this approach also removes the breakdown below 1 MHz it introduces a breakdown when going above that frequency.

A similar behavior is observed for the electric ring current as depicted in Fig. 6 (d) and the magnetic dipole in Fig. 6 (e). The errors in the current components correspond to the fields as predicted in Table II, and only the adaptive normalization (in addition to a stabilized RHS) fully removes the issues for all fields and for arbitrarily low frequencies.

The same is true for the spherical mode excitations TE_{11} and TM_{11} as shown in Fig. 6 (f) and (g), respectively. Note that the ad-hoc approach is not possible in this case but only the adaptive normalization can overcome the problem.

As the analysis so far showed that the problem lies in an insufficient accuracy of the solution components, another investigation is conducted for the sphere excited by a magnetic dipole: we vary the relative residual ϵ_{res} of the GMRES solver. In this numerical experiment, the ACA is not used and we employ $C = 1$ (to emphasize the effect of the residual). The results for the standard normalization in Fig. 7 (a) reveal that indeed by lowering the residual, the breakdown can be shifted to lower frequencies. However, even when employing a direct solver (LU-decomposition), the breakdown cannot be fully avoided. For large problems, iterative solvers become the only option; a typical choice for ϵ_{res} is around 1×10^{-3} to 1×10^{-4}. This

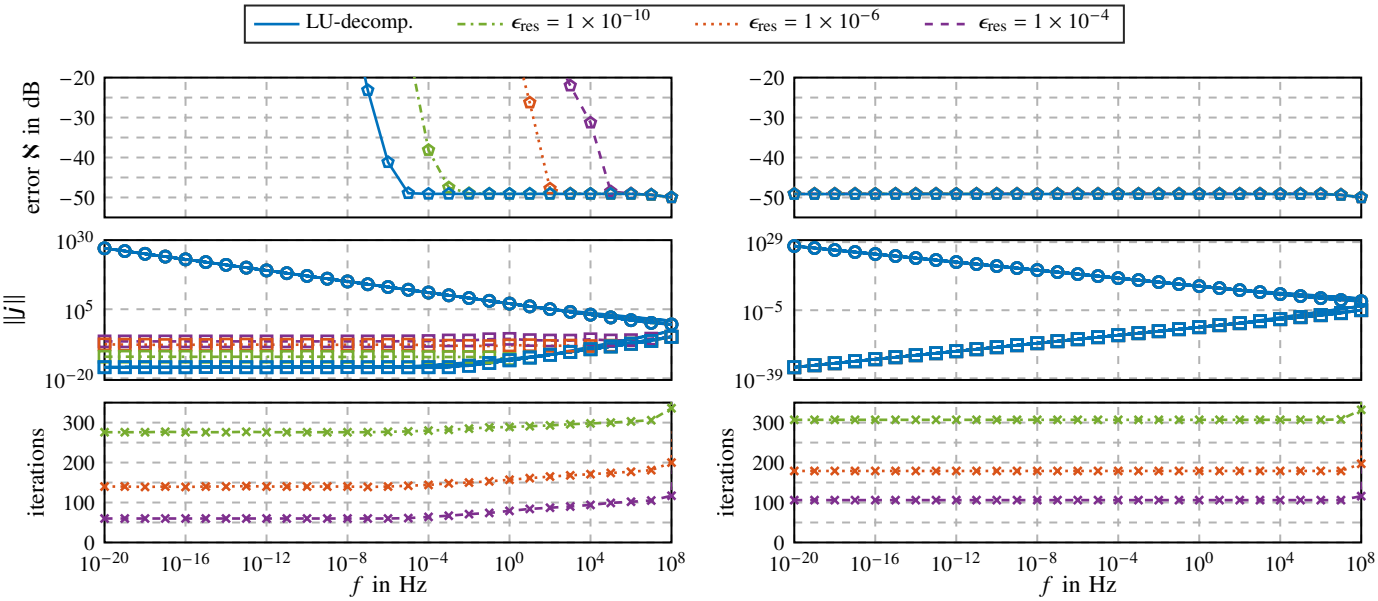

(a) standard normalization (b) this work: adaptive normalization

Fig. 7. Scattering from a sphere excited by a magnetic dipole using the standard and the adaptive frequency normalization employing different solvers: an LU-decomposition and GMRES with different relative residuals ϵ_{res}. Only the electric NF error is shown, no ACA is employed and $C = 1$.

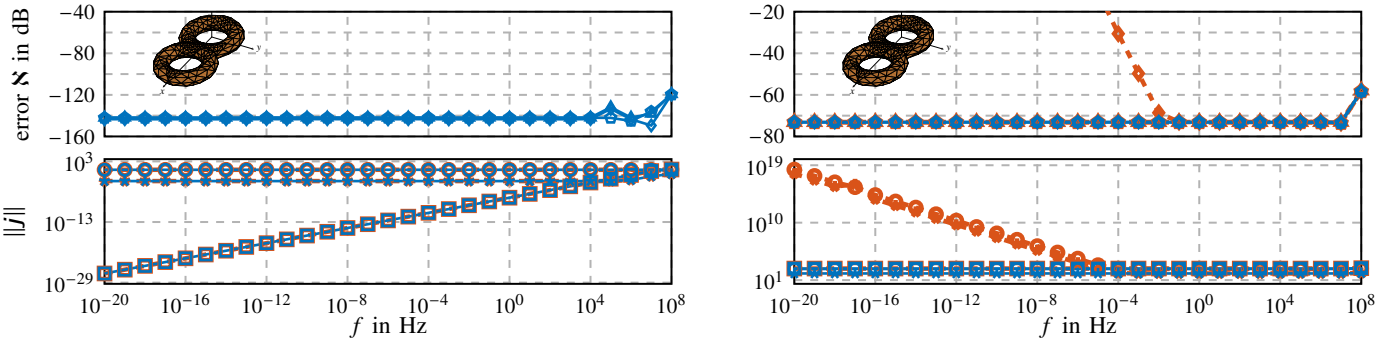

(a) plane wave (b) Hertzian dipole

Fig. 8. Scattering from a double torus: worst case errors of the FF, the electric, and the magnetic NF, as well as the scaling of the current components for different excitations. The HD is placed at $x = 0.8\,\text{m}$ and no ACA is used.

underlines the importance for using an adaptive normalization as shown in Fig. 7 (b), where we see that the error in the solution is dominated by the geometric approximation and discretization and not by the stopping criterion. Furthermore, the number of iterations remains constant when decreasing the frequency, whereas the iteration count for the standard normalization decreases with decreasing frequency: with the standard normalization only the solenoidal component is recovered, however, not the non-solenoidal component. Hence, the iterative solver only determines a part of the unknowns sufficiently accurately, but stops too early for the remaining unknowns resulting in the erroneous electric NF. Also note that separate residuals for solenoidal and non-solenoidal components are not possible (as the non-solenoidal component of the RHS depends on all current components) and if so, would lead to longer convergence times. Similarly, real and imaginary part of the RHS depend each on the real and the imaginary part of the current, thus, preventing a separate residual for real and imaginary part of the current without an approximation.

Fig. 9. Model of a Fokker Dr.I with an approximate wingspan of 7 m. The model is discretized with 196 280 triangles and 294 420 RWGs.

B. Scattering from Multiply-Connected Geometries

To validate our formulation also for multiply-connected geometries, we consider the double torus in Fig. 1 for a plane-wave and a Hertzian dipole excitation. The results in Fig. 8 demonstrate the effectiveness of our approach.

The results for the (PEC) model of a Fokker Dr.I shown in Fig. 9 excited by a Hertzian dipole in Fig. 10 highlight again

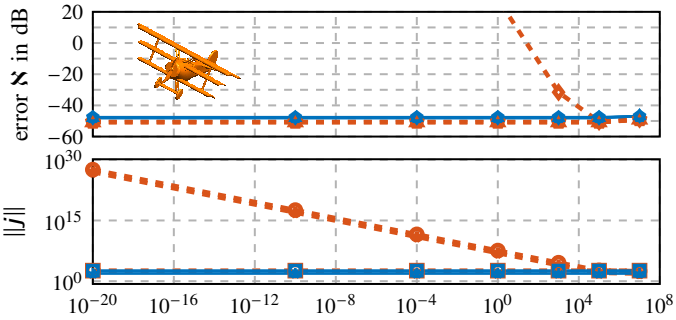

Fig. 10. Scattering from the model of a Fokker Dr.I excited by a Hertzian dipole.

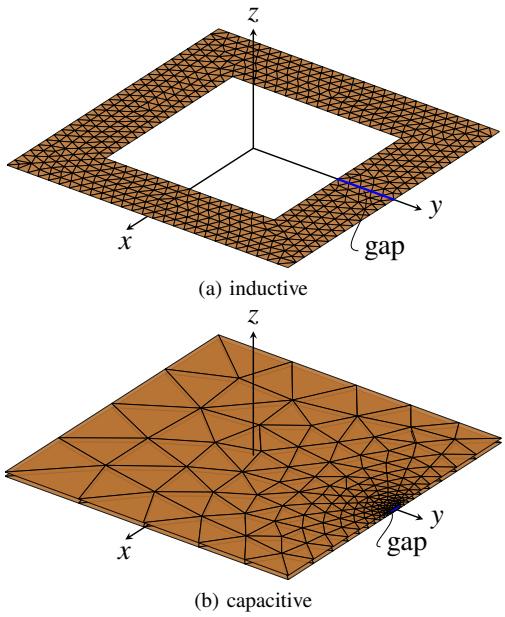

Fig. 11. Inductive and capacitive structure excited by voltage gaps (location highlighted in blue) (a) along positive y-axis and (b) in xy-plane.

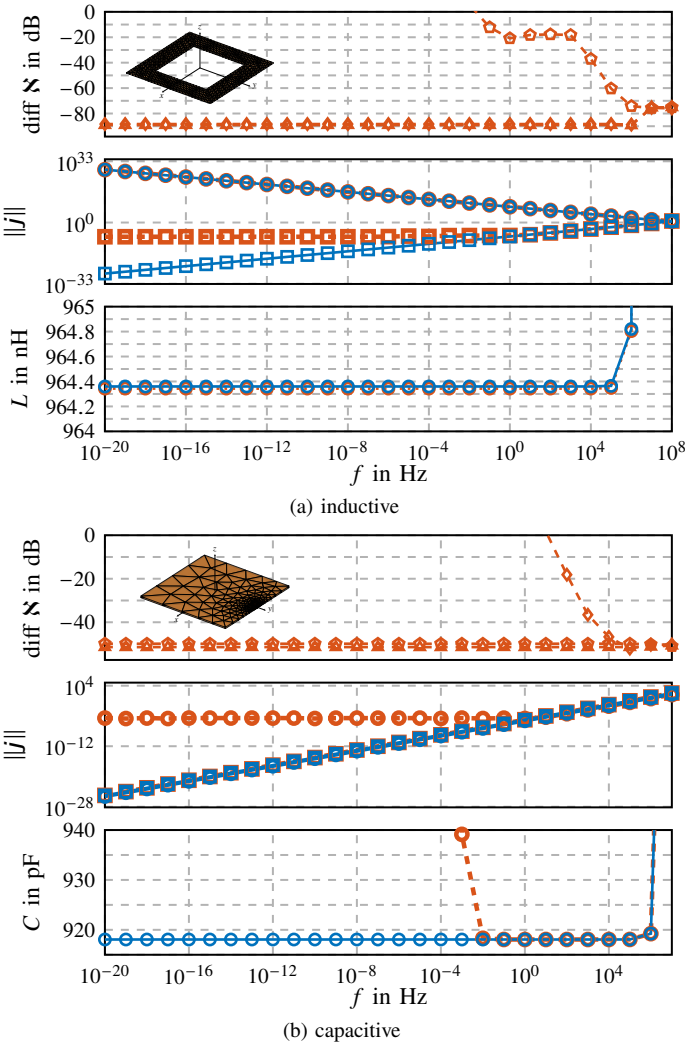

Fig. 12. Radiation from an inductive and a capacitive structure excited by a voltage gap excitation: comparison between the standard and the adaptive normalization scheme.

that the breakdown in accuracy can occur at relatively high frequencies but is fully overcome by the proposed scheme.

C. Inductive and Capacitive Gap Excitation

As a last example, we consider the voltage gap excitation of the capacitive and the inductive structure depicted in Fig. 11. The capacitive structure consist of two plates of size 1 m × 1 m separated by 0.01 m, where the non-uniformity of the mesh originates from the small size of the strip connecting the two plates. The inductive structure is a 1 m × 1 m ring with 0.25 m width. A comparison to the radiated fields when using the standard normalization is shown in Fig. 12. Clearly, for both structures only the adaptive scheme yields the physically correct scalings of the current components as given in Table V. For the inductive structure, the non-solenoidal current is incorrect resulting in a difference in the electric NF. Dually, for the capacitive structure, the solenoidal current is incorrect resulting in a difference in the magnetic NF, all in accordance with Table II. The determined inductivity of 964.3 nH agrees well with the 962.5 nH from a quasistatic simulation in Computer Simulation Technology Microwave Studio (CST MWS) [42]. Analogously, the determined capacitance of 918.05 pF agrees well with the 917.65 pF from an electrostatic simulation in CST MWS.

VI. Conclusion

We have shown that scaling coefficients in the quasi-Helmholtz preconditioners, which lead to a well-conditioned impedance matrix, do not necessarily lead to current solutions that allow an accurate determination of all fields. In fact, despite a well-conditioned matrix, the current components are in general solved for with different relative accuracies, which is for general excitations not sufficient. The numerical results demonstrated that the proposed adaptive frequency normalization method effectively resolves this effect for all excitations considered and, thus, allows for the accurate computation of near and far fields. In fact, depending on the structure and the specific excitation, standard approaches lead to inaccurately computed fields already in the MHz region, whereas with the proposed method, the scattered and radiated fields can be determined correctly ~~with an overall reduced number of iterations~~ down to the static limit. Given our theoretical considerations

and the wide range of studied excitations, we conclude that our method can stabilize the EFIE in the presence of arbitrary excitations.

Appendix A
Right-Hand Side Scalings

In order to derive real and imaginary part of the solenoidal and non-solenoidal components of the RHS for the excitations in Table III (i.e., for $k \to 0$), the corresponding excitation fields $\boldsymbol{e}^{\mathrm{ex}}$ are expressed via their currents $\boldsymbol{j}^{\mathrm{ex}}$ and $\boldsymbol{m}^{\mathrm{ex}}$ and the Green's function representation

$$\begin{aligned}\iint_\Gamma \boldsymbol{t}\cdot\boldsymbol{e}^{\mathrm{ex}}\,\mathrm{d}S(\boldsymbol{r}) = -\mathrm{j}\omega\mu \iint_\Gamma \boldsymbol{t}\cdot\iiint G\boldsymbol{j}^{\mathrm{ex}}\,\mathrm{d}V(\boldsymbol{r}')\,\mathrm{d}S(\boldsymbol{r})\\ -\mathrm{j}\frac{c\mu}{\omega}\iint_\Gamma \boldsymbol{t}\cdot\iiint \nabla'\cdot\boldsymbol{j}^{\mathrm{ex}}\nabla G\,\mathrm{d}V(\boldsymbol{r}')\,\mathrm{d}S(\boldsymbol{r})\\ +\iint_\Gamma \boldsymbol{t}\cdot\iiint \nabla G\times\boldsymbol{m}^{\mathrm{ex}}\,\mathrm{d}V(\boldsymbol{r}')\,\mathrm{d}S(\boldsymbol{r})\end{aligned} \tag{36}$$

using a Taylor series expansion of the Green's function

$$G = \frac{\mathrm{e}^{-\mathrm{j}kR}}{4\pi R} = \frac{1}{4\pi R}\sum_{q=0}^{\infty}\frac{(-\mathrm{j}kR)^q}{q!} \tag{37}$$

with the distance $R = |\boldsymbol{r}-\boldsymbol{r}'|$ between source point $\boldsymbol{r}'$ and observation point $\boldsymbol{r}$ and a Taylor series expansion of the gradient of the Green's function

$$\nabla G = \frac{\boldsymbol{R}}{4\pi R^3}\sum_{q=0}^{\infty}\frac{q-1}{q!}(-\mathrm{j}kR)^q \tag{38}$$

with $\boldsymbol{R} = \boldsymbol{r}-\boldsymbol{r}'$. We obtain the tabulated values by considering that the scalar potential contribution vanishes when tested by a solenoidal function, that is,

$$\iint_\Gamma \boldsymbol{t}\cdot\iiint \nabla'\cdot\boldsymbol{j}^{\mathrm{ex}}\nabla G\,\mathrm{d}V(\boldsymbol{r}')\,\mathrm{d}S(\boldsymbol{r}) = 0 \qquad \text{if} \quad \nabla_\Gamma\cdot\boldsymbol{t} = 0 \tag{39}$$

that a constant vector tested by a solenoidal function vanishes, that is,

$$\iint_\Gamma \boldsymbol{t}\cdot\boldsymbol{c}\,\mathrm{d}S(\boldsymbol{r}') = 0 \qquad \text{if} \quad \nabla_\Gamma\cdot\boldsymbol{t} = 0 \text{ and } \boldsymbol{c} = \mathrm{const} \tag{40}$$

that a solenoidal excitation current tested by a solenoidal function vanishes, that is,

$$\iint_\Gamma \boldsymbol{t}\cdot\iiint \boldsymbol{j}^{\mathrm{ex}}\,\mathrm{d}V(\boldsymbol{r}')\,\mathrm{d}S(\boldsymbol{r}) = 0 \qquad \text{if} \quad \nabla_\Gamma\cdot\boldsymbol{t} = 0 \text{ and } \nabla\cdot\boldsymbol{j}^{\mathrm{ex}} = 0 \tag{41}$$

that [43]

$$\iint_\Gamma \boldsymbol{t}\cdot\iiint \frac{\boldsymbol{R}}{R^3}\times\boldsymbol{m}^{\mathrm{ex}}\,\mathrm{d}V(\boldsymbol{r}')\,\mathrm{d}S(\boldsymbol{r}) = 0 \qquad \text{if} \quad \nabla_\Gamma\cdot\boldsymbol{t} = 0 \text{ and } \nabla\cdot\boldsymbol{m}^{\mathrm{ex}} = 0 \tag{42}$$

and

$$\iint_\Gamma \boldsymbol{t}\cdot\iiint \boldsymbol{R}\times\boldsymbol{m}^{\mathrm{ex}}\,\mathrm{d}V(\boldsymbol{r}')\,\mathrm{d}S(\boldsymbol{r}) = 0 \qquad \text{if} \quad \nabla_\Gamma\cdot\boldsymbol{t} = 0 \text{ and } \nabla\cdot\boldsymbol{m}^{\mathrm{ex}} = 0\,. \tag{43}$$

Appendix B
Scaling of TE and TM Modes

For a combination of TE_{mn} modes with largest appearing order $n = N_{\mathrm{TE}}$ and TM_{mn} modes with largest appearing order $n = N_{\mathrm{TM}}$, the ratio w of solenoidal and non-solenoidal tested field vectors scales as

$$w = \frac{\|\boldsymbol{e}_{\mathrm{sol,hsol}}\|}{\|\boldsymbol{e}_{\mathrm{nsol}}\|} = \frac{O\left(k^{-(N_{\mathrm{TM}}-1)} + k^{-N_{\mathrm{TE}}}\right)}{O\left(k^{-(N_{\mathrm{TM}}+1)} + k^{-N_{\mathrm{TE}}}\right)} \quad \text{for } k \to 0\,. \tag{44}$$

For $N_{\mathrm{TE}} \geq N_{\mathrm{TM}} + 1$, we clearly have

$$w = O(1)\,. \tag{45}$$

For $N_{\mathrm{TE}} < N_{\mathrm{TM}} + 1$ we have

$$w = \frac{O\left(k^{-(N_{\mathrm{TM}}-1)} + k^{-N_{\mathrm{TE}}}\right)}{O\left(k^{-(N_{\mathrm{TM}}+1)}\right)}\,. \tag{46}$$

In the case $N_{\mathrm{TE}} = N_{\mathrm{TM}}$, this leads to $w = O(k)$ and for all $N_{\mathrm{TE}} = N_{\mathrm{TM}} - g$ with $g \geq 1$, it leads to $w = O(k^2)$. In consequence, we have

$$O(1) \leq w \leq O(k^2) \tag{47}$$

for all possible combinations of N_{TE} and N_{TM}.

For the special case of scattering from a sphere placed in the origin, we have

$$w = \frac{\|\boldsymbol{e}_{\mathrm{sol,hsol}}\|}{\|\boldsymbol{e}_{\mathrm{nsol}}\|} = \frac{\left(k^{-N_{\mathrm{TE}}}\right)}{O\left(k^{-(N_{\mathrm{TM}}+1)} + k^{-N_{\mathrm{TE}}}\right)}\,. \tag{48}$$

Again, for $N_{\mathrm{TE}} \geq N_{\mathrm{TM}} + 1$, this leads to $w = O(1)$. On the other hand, for $N_{\mathrm{TE}} < N_{\mathrm{TM}} + 1$, we have the case $N_{\mathrm{TE}} = N_{\mathrm{TM}}$ leading to $w = O(k)$ and the cases where $N_{\mathrm{TE}} = N_{\mathrm{TM}} - g$ with $g \geq 1$ resulting in

$$w = O\left(k^{(g+1)}\right)\,, \tag{49}$$

which is a case not satisfying (47).

References

[1] D. R. Wilton and A. W. Glisson, "On improving the electric field integral equation at low frequencies," *Proc. URSI Radio Sci. Meet. Dig*, vol. 24, p. 33, 1981.

[2] J. Mautz and R. Harrington, "An E-Field Solution for a Conducting Surface Small or Comparable to the Wavelength," *IEEE Trans. Antennas Propag.*, vol. 32, no. 4, pp. 330–339, Apr. 1984.

[3] W.-L. Wu, A. W. Glisson, and D. Kajfez, "A Study of Two Numerical Solution Procedures for the Electric Field Integral Equation at Low Frequency," *Appl. Comput. Electromagn. Soc. J.*, vol. 10, no. 3, pp. 69–80, Jan. 1995.

[4] M. Burton and S. Kashyap, "A Study of a Recent, Moment-Method Algorithm that is Accurate to Very Low Frequencies," *Appl. Comput. Electromagn. Soc. J.*, vol. 10, pp. 58–68, 1995.

[5] F. P. Andriulli, K. Cools, I. Bogaert, and E. Michielssen, "On a Well-Conditioned Electric Field Integral Operator for Multiply Connected Geometries," *IEEE Trans. Antennas Propag.*, vol. 61, no. 4, pp. 2077–2087, Apr. 2013.

[6] G. Vecchi, "Loop-Star Decomposition of Basis Functions in the Discretization of the EFIE," *IEEE Trans. Antennas Propag.*, vol. 47, no. 2, pp. 339–346, Feb. 1999.

[7] T. F. Eibert, "Iterative-Solver Convergence for Loop-Star and Loop-Tree Decompositions in Method-of-Moments Solutions of the Electric-Field Integral Equation," *IEEE Antennas Propag. Mag.*, vol. 46, no. 3, pp. 80–85, Jun. 2004.

[8] F. P. Andriulli, "Loop-Star and Loop-Tree Decompositions: Analysis and Efficient Algorithms," *IEEE Trans. Antennas Propag.*, vol. 60, no. 5, pp. 2347–2356, May 2012.

[9] J. R. Mautz and R. F. Harrington, "A New E-Field Solution for a Conducting Surface Small or Comparable to the Wavelength," Syracuse Univ. NY Dept. Elect. Comput. Eng., Tech. Rep., Sep. 1982.

[10] B. Hofmann, T. F. Eibert, F. P. Andriulli, and S. B. Adrian, "A Low-Frequency Stable, Excitation Agnostic Discretization of the Right-Hand Side for the Electric Field Integral Equation on Multiply-Connected Geometries," *TechRxiv*, Oct. 2022, accepted to IEEE Trans. Antennas Propag. DOI: 10.36227/techrxiv.21203006.

[11] ——, "Low-Frequency Stable Discretization of the Electric Field Integral Equation Based on Poincaré's Lemma," in *Proc. IEEE Antennas Propag. Soc. Int. Symp. URSI Nat. Radio Sci. Meeting*, Singapore: IEEE, Dec. 2021.

[12] ——, "Efficient Combination of Scalar-Potential Representations of Solenoidal Functions and Quasi-Helmholtz Projectors," in *Proc. 16th Eur. Conf. Antennas Propag. (EuCAP)*, Madrid, Spain, Mar. 2022.

[13] T. L. Chhim, A. Merlini, L. Rahmouni, J. E. O. Guzman, and F. P. Andriulli, "Eddy Current Modeling in Multiply Connected Regions via a Full-Wave Solver Based on the Quasi-Helmholtz Projectors," *IEEE Open J. Antennas Propag.*, vol. 1, pp. 534–548, Sep. 2020.

[14] Z. Qian and W. C. Chew, "An Augmented Electric Field Integral Equation for Low Frequency Electromagnetic Analysis," in *Proc. IEEE Antennas Propag. Soc. Int. Symp. URSI Nat. Radio Sci. Meeting*, San Diego, CA, Jul. 2008, pp. 1–4.

[15] ——, "Enhanced A-EFIE With Perturbation Method," *IEEE Trans. Antennas Propag.*, vol. 58, no. 10, pp. 3256–3264, Oct. 2010.

[16] C. L. Epstein and L. Greengard, "Debye Sources and the Numerical Solution of the Time Harmonic Maxwell Equations," *Commun. Pure Appl. Math.*, vol. 63, no. 4, pp. 413–463, Dec. 2009.

[17] J. Li, D. Dault, B. Liu, Y. Tong, and B. Shanker, "Subdivision Based Isogeometric Analysis Technique for Electric Field Integral Equations for Simply Connected Structures," *J. Comp. Physics*, vol. 319, pp. 145–162, Aug. 2016.

[18] F. Vico, M. Ferrando, L. Greengard, and Z. Gimbutas, "The Decoupled Potential Integral Equation for Time-Harmonic Electromagnetic Scattering," *Commun. Pure Appl. Math.*, vol. 69, no. 4, pp. 771–812, Apr. 2016.

[19] J. S. Zhao and W. C. Chew, "Integral Equation Solution of Maxwell's Equations from Zero Frequency to Microwave Frequencies," *IEEE Trans. Antennas Propag.*, vol. 48, no. 10, pp. 1635–1645, Oct. 2000.

[20] M. A. Echeverri Bautista, M. A. Francavilla, F. Vipiana, and G. Vecchi, "A Hierarchical Fast Solver for EFIE-MoM Analysis of Multiscale Structures at Very Low Frequencies," *IEEE Trans. Antennas Propag.*, vol. 62, no. 3, pp. 1523–1528, Mar. 2014.

[21] S. B. Adrian, F. P. Andriulli, and T. F. Eibert, "A Hierarchical Preconditioner for the Electric Field Integral Equation on Unstructured Meshes Based on Primal and Dual Haar Bases," *J. Comp. Physics*, vol. 330, pp. 365–379, Feb. 2017.

[22] B. Hofmann, T. F. Eibert, F. P. Andriulli, and S. B. Adrian, "Low-Frequency-Stabilized Electric Field Integral Equation on Topologically Non-Trivial Geometries for Arbitrary Excitations," in *Proc. IEEE Antennas Propag. Soc. Int. Symp. URSI Nat. Radio Sci. Meeting*, Denver, CO, Jul. 2022.

[23] ——, "Towards a Low-Frequency-Stabilized Electric Field Integral Equation on Simply-Connected Geometries for Arbitrary Excitations," in *URSI Atlantic / Asia-Pacific Radio Sci. Conf.*, Gran Canaria, Spain, May 2022.

[24] J. R. Mautz and R. F. Harrington, "H-Field, E-Field, and Combined-Field Solutions for Conducting Bodies of Revolution," *Int. J. Electron. Commun.*, vol. 32, pp. 157–164, Apr. 1978.

[25] W. A. Johnson, D. R. Wilton, and R. M. Sharpe, "Modeling Scattering From and Radiation by Arbitrary Shaped Objects with the Electric Field Integral Equation Triangular Surface Patch Code," *Electromagnetics*, vol. 10, no. 1-2, pp. 41–63, Jan. 1990.

[26] A. Buffa and S. Christiansen, "The Electric Field Integral Equation on Lipschitz Screens: Definitions and Numerical Approximation," *Numer. Math.*, vol. 94, no. 2, pp. 229–267, Apr. 2003.

[27] F. P. Andriulli, K. Cools, H. Bagci, F. Olyslager, A. Buffa, S. Christiansen, and E. Michielssen, "A Multiplicative Calderon Preconditioner for the Electric Field Integral Equation," *IEEE Trans. Antennas Propag.*, vol. 56, no. 8, pp. 2398–2412, Aug. 2008.

[28] S. B. Adrian, A. Dély, D. Consoli, A. Merlini, and F. P. Andriulli, "Electromagnetic Integral Equations: Insights in Conditioning and Preconditioning," *IEEE Open J. Antennas Propag.*, pp. 1143–1174, Oct. 2021.

[29] I. Bogaert, K. Cools, F. P. Andriulli, and H. Bağcı, "Low-Frequency Scaling of the Standard and Mixed Magnetic Field and Müller Integral Equations," *IEEE Trans. Antennas Propag.*, vol. 62, no. 2, pp. 822–831, Feb. 2014.

[30] J. E. Hansen, Ed., *Spherical Near-Field Antenna Measurements*. The Institution of Engineering and Technology, Michael Faraday House, Six Hills Way, Stevenage SG1 2AY, UK: IET, Jan. 1988, repr. 2008.

[31] L. N. Trefethen and D. Bau, *Numerical Linear Algebra*. Philadelphia, PA 19104-2688: SIAM, Jan. 1997.

[32] G. W. Stewart, "A Krylov–Schur Algorithm for Large Eigenproblems," *SIAM J. Matrix Anal. Appl.*, vol. 23, no. 3, pp. 601–614, Jan. 2002.

[33] O. Steinbach, *Numerical Approximation Methods for Elliptic Boundary Value Problems*. New York, NY: Springer New York, 2008.

[34] Y. Saad, *Iterative Methods for Sparse Linear Systems*, 2. Edition. Philadelphia: Society for Industrial and Applied Mathematics, Apr. 1, 2003.

[35] Y. Saad and M. H. Schultz, "GMRES: A Generalized Minimal Residual Algorithm for Solving Nonsymmetric Linear Systems," *SIAM J. Sci. Stat. Comput.*, vol. 7, no. 3, pp. 856–869, Jul. 1986.

[36] P. Sonneveld and M. B. van Gijzen, "IDR(s): A Family of Simple and Fast Algorithms for Solving Large Nonsymmetric Systems of Linear Equations," *SIAM J. Sci. Comput.*, Nov. 2008.

[37] G. L. Sleijpen and D. R. Fokkema, "BiCGstab(L) for Linear Equations Involving Unsymmetric Matrices with Complex Spectrum," *Electron. Trans. Num. Anal.*, vol. 1, pp. 11–32, 1993.

[38] K. Zhao, M. Vouvakis, and J.-F. Lee, "The Adaptive Cross Approximation Algorithm for Accelerated Method of Moments Computations of EMC Problems," *IEEE Trans. Electromagn. Compat.*, vol. 47, no. 4, pp. 763–773, Nov. 2005.

[39] M. Bebendorf, *Hierarchical Matrices: A Means to Efficiently Solve Elliptic Boundary Value Problems*. Berlin: Springer, Jun. 2008.

[40] J.-M. Jin, *Theory and Computation of Electromagnetic Fields*, Second edition. Hoboken, New Jersey: John Wiley & Sons, Inc, 2015.

[41] B. Hofmann, *SphericalScattering*, version v.0.1.1, Aug. 2022. [Online]. Available: https://doi.org/10.5281/zenodo.7026709.

[42] CST Computer Simulation Technology, *Microwave Studio*, Darmstadt, Germany, 2022. [Online]. Available: https://www.cst.com.

[43] S. Y. Chen, Weng Cho Chew, J. M. Song, and Jun-Sheng Zhao, "Analysis of Low Frequency Scattering from Penetrable Scatterers," *IEEE Trans. Geosci. Remote Sens.*, vol. 39, no. 4, pp. 726–735, Apr. 2001.